

This is an Open Access document downloaded from ORCA, Cardiff University's institutional repository:<https://orca.cardiff.ac.uk/id/eprint/93616/>

This is the author's version of a work that was submitted to / accepted for publication.

Citation for final published version:

Marzano, Frank, Picciotti, Errico, Di Fabio, Saverio, Montopoli, Mario, Mereu, Luigi, Degruyter, Wim, Bonadonna, Costanza and Ripepe, Maurizio 2016. Near-real-time detection of tephra eruption onset and mass flow rate using microwave weather radar and infrasonic arrays. *IEEE Transactions on Geoscience and Remote Sensing* 54 (11), pp. 6292-6306. 10.1109/TGRS.2016.2578282

Publishers page: <http://dx.doi.org/10.1109/TGRS.2016.2578282>

Please note:

Changes made as a result of publishing processes such as copy-editing, formatting and page numbers may not be reflected in this version. For the definitive version of this publication, please refer to the published source. You are advised to consult the publisher's version if you wish to cite this paper.

This version is being made available in accordance with publisher policies. See <http://orca.cf.ac.uk/policies.html> for usage policies. Copyright and moral rights for publications made available in ORCA are retained by the copyright holders.



# Near Real-Time Detection of Tephra Eruption Onset and Mass Flow Rate using Microwave Weather Radar and **Infrasonic** Array

Frank S. Marzano, *Fellow, IEEE*, Errico Picciotti, Saverio Di Fabio, Mario Montopoli, Luigi Mereu, Wim Degruyter, Costanza Bonadonna and Maurizio Ripepe

**Abstract**— During an eruptive event the near real-time monitoring of volcanic explosion onset and its mass flow rate is a key factor to predict ash plume dispersion and to mitigate risk to air traffic. Microwave weather radars have proved to be a fundamental instrument to derive eruptive source parameters. We extend this capability to include an early-warning detection scheme within the overall Volcanic Ash Radar Retrieval (VARR) methodology. This scheme, called volcanic ash detection (VAD) algorithm, is based on a hybrid technique using both fuzzy logic and conditional probability. Examples of VAD applications are shown for some case studies, including the Icelandic Grímsvötn eruption in 2011, the Eyjafjallajökull eruption in 2010 and the Italian Mt. Etna volcano eruption in 2013. Estimates of the eruption onset from the radar-based VAD module are compared with infrasonic array data. One-dimensional numerical simulations and analytical model estimates of mass flow rate are also discussed and intercompared with sensor-based retrievals. Results confirm in all cases the potential of microwave weather radar for ash plume monitoring in near real-time and its complementarity with infrasonic array for early-warning system design.

**Index Terms**—Volcanic ash, Weather radar, Microwave remote sensing, Detection algorithm.

## I. INTRODUCTION

During an explosive volcanic eruption, tephra particles are injected into the atmosphere and may severely affect air traffic and local environment, as clearly demonstrated by the Icelandic 2010 Eyjafjallajökull eruption [1]-[3]. For prevention and protection needs, a key issue is to deliver a prompt early warning of the on-going volcanic eruption and to estimate the Mass Flow Rate (MFR) to properly initialize ash dispersion forecasting models [4]-[6]. Satellite radiometry is a well-established method for the dispersed ash plume detection

and monitoring [7]. However, estimates from spaceborne visible-infrared radiometers may be limited, depending on the sensor and platform, to daylight periods, few overpasses per day, optically thin ash clouds and, if present, obscured by water clouds [8], [9].

Complementary to satellite sensors, a ground-based microwave (MW) weather radar represents nowadays a well-established technique to monitor quantitatively a volcanic eruption and its tephra ejection [10]-[12]. Weather radars can provide a three-dimensional (3D) volume of eruption source parameters (e.g., plume height, particle size distribution, MFR) as well as mass concentration and velocity fields, at any time during the day or night with a periodicity of 5-to-15 minutes and a spatial resolution less than a kilometer even in the presence of water clouds [13], [14]. The major limitations of plume radar retrieval are its limited spatial coverage (say less than 150 km radius around the radar site), its poor sensitivity to fine ash particles (say less than a diameter of 50 microns) and the relatively long time for completing a volume scan (order of several minutes). This implies, for example, that the top of the ash column above the emission source might be only partially detected and the extension of the horizontally-spreading plume may be underestimated and tracked for a relatively short distance [15], [39].

For a quantitative estimation of ash, an algorithm, called Volcanic Ash Radar Retrieval (VARR), has been developed in the recent years using radar systems operating at S, C and X band at single and dual polarization [16], [17]. Note that even though the acronym VARR refers to ash estimation by microwave radars, the latter are in general sensitive to all tephra fragments, including lapilli (2-64 mm) and blocks and bombs (>64 mm). However, the term “ash” is so widely exploited that we will use it in place of tephra thus intending all volcanic particles injected into the atmosphere irrespective of size, shape

Manuscript received March 22, 2016. This work has been partially funded by the FUTUREVOLC project (Grant agreement n. 308377) within the European Union’s FP7/2007-2013 program. The research leading to these results has also received funding from the APHoRISM project (Grant agreement n. 606738) within FP7/2007-2013 program.

F. S. Marzano, L. Mereu, and M. Montopoli are with the Dipartimento di Ingegneria dell’Informazione (DIET), Sapienza Università di Roma, 00184 Rome, Italy, and also with the CETEMPS Center of Excellence, Università dell’Aquila, 67100 L’Aquila, Italy (e-mail: marzano@diet.uniroma1.it; mereu@diet.uniroma1.it). M. Montopoli is currently with the National Research Council (CNR), ISAC, Rome, Italy (m.montopoli@isac.cnr.it).

E. Picciotti and S. Di Fabio are with CETEMPS Center of Excellence, Università dell’Aquila, 67100 L’Aquila, Italy and HIMET Srl, L’Aquila, Italy (e-mail: saverio.difabio@aquila.infn.it, errico.picciotti@himet.it)

W. Degruyter is with Institute of Geochemistry and Petrology, Department of Earth Sciences, ETH Zurich. (wim.degruyter@erdw.ethz.ch)

C. Bonadonna is with the Department of Earth Sciences, University of Geneva, 1205 Geneva, Switzerland (e-mail: Costanza.Bonadonna@unige.ch).

M. Ripepe is with the Dipartimento di Scienze della Terra - University of Florence, Florence (Italy) (email: maurizio.ripepe@unifi.it)

Color versions of one or more of the figures in this paper are available online at <http://ieeexplore.ieee.org>.

and composition, if not otherwise specified. The VARR theoretical background, application and validation have been extensively described in previous works [12]. One key issue, which is still open, is its extension to the detection of ash plume onset in order to be used within an early warning system for volcanic hazard prediction. In this respect, weather radars can be complementary to the other early warning instruments like tremor detection networks, cloud detections based on Global Positioning System (GPS) receiver networks, thermal and visible cameras, and infrasonic arrays (e.g., [18], [19], [25]). In particular, infrasonic airwave, produced by volcanic eruptions (usually at frequencies lower than 20 Hz), can be detected as an atmospheric pressure field variation also at remote distances [20]-[22]. Arrays of infrasonic sensors, deployed as small aperture (~100 m) antennas and distributed at various azimuths around a volcano, show tremendous potential for enhanced event detection and localization. At short distances (<10 km) from the source, the almost constant velocity of sound makes precise localization (within a few tens of meters accuracy) possible. With respect to other systems, infrasound is also largely unaffected by cloud cover and does not rely on line-of-sight view of vents (e.g. [19], [25]), as is the case with satellite or radar observations.

The goal of this work is to extend VARR by including a volcanic ash detection (VAD) module and designing an overall scheme for ash plume monitoring in near-real time providing eruption onset time, plume tracking and geophysical products. The focus is on the methodological issues more than its statistical validation so that examples of VAD application are shown for specific test cases. Using data from recent volcanic eruptions, time series of infrasonic array and radar acquisitions in the proximity of the volcanic vent are used together to understand the potentiality of combining the two ground-based measurements for eruption onset early warning. Detection and estimation of MFR are also evaluated and compared with estimates from analytical equations, 1D volcanic plume models and infrasound-based methods.

The basic idea of VAD is that during standard operations the radar algorithm is set into a “meteorological mode” (devoted to monitoring precipitating water cloud echoes), but a special processing is envisaged at the locations where potentially active volcanoes are present within the radar coverage area. VAD continually runs for each radar volume acquisition. Whenever the VAD detection test is passed (that is, an eruption is confirmed from VAD radar data analysis), the VARR data processing switches into an “ash mode” and the tracking module is activated (manually or automatically, depending on the system). Note that near real-time tracking of volcanic cloud dispersal represents an essential datum both for aviation and civil safety. Early warning advisory can be spread to the local authorities if the ash plume trajectory threatens some sensitive areas (e.g., airports, aviation routes, critical infrastructures, towns and metropolitan regions). In addition, the indication of the velocity of the transported plume provided by the tracking module can be a useful and alternative way for the retrieval of the plume altitude given the knowledge of the velocity- altitude profile obtained for example by radiosoundings and/or

meteorological forecasts.

The paper is organized as follows. Section II will provide an overview of VARR block diagram, including the VAD module. The latter will be described in detail using a hybrid fuzzy logic and conditional probability approach. By exploiting available data, Section III and IV will show examples of VAD applications for the Icelandic Grímsvötn eruption occurred in 2011 and the Italian Mt. Etna volcano eruption occurred in 2013. In the latter event radar-based retrievals will be compared with infrasonic array data to interpret the respective signatures and explore their synergy. In section V VARR-based retrievals of the MFR at the vent will be analyzed for the May 5-10 period of the 2010 Eyjafjallajökull eruption by comparing with estimates from 1D numerical model, analytical formula and infrasonic array. Section VI will draw conclusions and future work recommendations.

## II. DESIGNING VOLCANIC ASH RADAR RETRIEVAL

The objective of this section is to illustrate an overall algorithm for MW weather radar polarimetric retrieval of volcanic ash plumes, including 4 major stages: detection, tracking, classification and estimation of ash (i.e. in our context all volcanic particles injected into the atmosphere irrespective of size, shape and composition). The underlying concepts will be illustrated by sketching the underpinning philosophy and the basic theory, referring to previous works where possible for the discussion of tracking, classification and estimation modules [12]. Only the detection module will be described in detail in Sect. II.B since it is the innovative module of this work.

The basic assumption in this work is that, in a given radar site, we have at disposal a set of variables at a specific frequency band (e.g., S, C and X band) at single or dual polarization with a given range, azimuth and elevation resolution (e.g., 250 m, 1° and 1°, respectively). The latter defines the so called radar resolution bin and for each bin we can introduce a polarimetric radar observable vector  $\mathbf{z}_m = [Z_{hhm}, Z_{drms}, K_{dpm}, \rho_{hv}, L_{drm}]$  where  $Z_{hhm}$  is the measured copolar reflectivity factor,  $Z_{drm}$  is the differential reflectivity,  $K_{dpm}$  is the differential phase shift,  $\rho_{hv}$  is copolar correlation (modulus) coefficient and  $L_{drm}$  is linear depolarization ratio. Since the availability of all these observables is not always guaranteed, depending on the system capability, some of them can be discarded from the analysis thus impacting the estimation accuracy. Details on the exploitation of dual-polarization and single-polarization radar systems can be found in [17] and [23]. All modules of VARR are supposed to operate on a volume-bin basis, whereas the use of spatial texture processing is foreseen, but not discussed here.

### A. Overall VARR scheme

The volcanic ash radar retrieval algorithm for polarimetric microwave radars is, in a very general context, structured in the following 4 main modules, shown in Fig. 1:

1. *Volcanic Ash Detection* (VAD) is detecting the ash plume onset from measured  $\mathbf{z}_m$ . The VAD algorithm is mainly devoted to characterize the typical ash radar signature,

possibly separating the radar bins affected by ash from those mainly interested by meteorological targets.

2. *Volcanic Ash Tracking* (VAT) is tracking the ash plume dispersion from measured  $\mathbf{z}_m$  within the radar coverage area. The VAT algorithms are the basis of monitoring and nowcasting the displacement of the ash mass in space and time.
3. *Volcanic Ash Classification* (VAC) is classifying ash particle class from measured  $\mathbf{z}_m$  within each radar bin in terms of particle's size, shape and orientation. The VAC module is based on the Maximum a Posteriori Probability criterion trained by a forward particle microwave scattering model.
4. *Volcanic Ash Estimation* (VAE) is estimating the ash concentration, fall rate, ash mean diameter and other volcanic products from the measured  $\mathbf{z}_m$  within each radar resolution bin.

**Fig. 1** shows a flowchart of the VARR scheme. The VAD and VAT modules can be supported by the integration of other available measurements, e.g. remote sensing data from spaceborne infrared radiometers, ground-based infrasonic arrays and lidars or in situ data, such as ash disdrometers or human inspections. On the other hand, VAC and VAE modules are fed by the forward microphysical-electromagnetic scattering models ingesting information about weather radar instrumental characteristics and possible in situ sampling of previous eruptions.

The VAD module will be described in the next section being the main objective of this work.

The VAT module takes as input the detection of the ash plume target and tracks it in time and space. In order to accomplish this task, a phase-based correlation technique (PCORR), well described in [24] and here only summarized, is used for this purpose. In order to estimate the displacement field, the PCORR algorithm exploits the comparison between two consecutive radar images, typically the Constant Altitude Plan Position Indicator (CAPPI) but applicable to any radar observed or estimated field  $F_{rad}$ . The displacement field is expressed by the horizontally motion vector  $\mathbf{V}(x,y)$  for each position  $(x,y)$  in the horizontal plane and whose Cartesian components  $u(x,y)$  and  $v(x,y)$  are used within an advection scheme to forecast the next radar image [24], [41]:

$$\hat{F}_{rad}(x, y, t + n\Delta t) = F_{rad}(x - u \cdot n\Delta t, y - v \cdot n\Delta t, t) \quad (1)$$

where  $t$  is the current time,  $\Delta t$  is the time step of radar acquisition (e.g., 5, 10 or 15 minutes) and  $n\Delta t$  is the lead time with respect to current time (e.g., 30 or 60 minutes in advance). The estimate of  $u$  and  $v$  components is carried out by computing the normalized Fourier transform of the spatial cross-correlation function  $S_{F_{cx}}(\Delta x, \Delta y)$  and by extracting the spatial shift  $(\Delta x, \Delta y)$  from the phase component of  $S_{F_{cx}}$ .

The frequency-domain approach improves the accuracy of motion directions and magnitude estimates by avoiding saturation effects in proximity of the correlation function multiple maxima. The limitations of PCORR, applied as described, are that: i) when applied to the whole radar image it

can provide only one motion vector per image thus implicitly supposing a steady state field; ii) sources and sinks of radar observables are not considered so that the field is displaced but not modified in its value. These issues can be partially addressed by resorting to a spatially-adaptive segmentation of the observed radar field to generate a spatially-variable advection field. This approach can forecast the rotation and deformation of the observed field and has been successfully applied to atmospheric precipitation on a relatively large scale, even though physical models of sources and sinks are not taken into account [41]. By comparing the nowcasted and the actual reflectivity maps, the accuracy of the predicted field decreases, as expected, with the increase of the lead time  $n\Delta t$ ; percentage errors of 75% can be typically obtained at 0.5 hour and of 60% at 1 hour, but a detailed analysis is beyond the scopes of this work.

The VAC module is widely described in [16] and [17] and here only summarized. Ash category classification is carried out by applying the Bayesian theory in a supervised manner, that is we evaluate the posterior probability density function (PDF) by using the forward microphysical scattering model [16], [12]. When maximizing the posterior PDF, the method is called Maximum A posteriori Probability (MAP) and the estimated ash class  $c_a$  at each time step and radar bin is expressed by [16]:

$$\hat{c}_a = Mode_c\{p(c_a|\mathbf{z}_m)\} = Mode_c\{p(\mathbf{z}_m|c_a)p(c_a)/p(\mathbf{z}_m)\} \quad (2)$$

where  $p$  are the probability density functions,  $Mode_c$  is the modal operator and  $\mathbf{z}_m$  polarimetric radar observable vector, being  $p(c_a|\mathbf{z}_m)$ ,  $p(\mathbf{z}_m|c_a)$  and  $p(c_a)$  the posterior, likelihood and *a priori* PDFs, respectively. The ash class  $c_a$  is usually provided in terms of size (i.e., fine ash: <63  $\mu\text{m}$ , coarse ash: 63  $\mu\text{m}$  -2 mm, lapilli: 2-64 mm together with blocks and bombs larger than 64 mm) and mass concentration category (e.g., low: average around 0.1  $\text{g}/\text{m}^3$ , medium: average around 1  $\text{g}/\text{m}^3$ , high: average around 5  $\text{g}/\text{m}^3$ ). The *a priori* PDF  $p(c_a)$  is used to insert available information on the requirements that make the existence of the class  $c_a$  likely in a given environmental condition. The *a priori* PDF is typically set uniform unless there is evidence of prevailing ash class. A usual simplifying assumption of MAP is to introduce a multi-dimensional Gaussian PDF model in order to reduce (2) to the minimization of a quadratic metrics, that is the squared generalized distance between the available polarimetric measurement and the corresponding class centroids, obtained from the forward microphysical scattering model [16]. The advantage of a supervised Bayesian approach is the flexibility and rigorousness to deal with all data, but, on the other hand, it strongly relies on the accuracy of the forward training model.

The VAE module is well described in [16], [17] and [12] so that here is only summarized. The Bayesian approach can be also used, in principle, for the estimation of physical source parameters. In case we are able to assume a function model  $f_{est}$  to relate the predicted parameter with available measurements, then the Bayesian method reduces to statistical regression so that the estimated volcanic ash parameter  $P_a$  is expressed by [17]:

$$\hat{p}_a = f_{est}(\mathbf{z}_m; \mathbf{r} | \hat{c}_a) \quad (3)$$

where  $\mathbf{r}$  is the vector of unknown regression coefficients which are found by a minimum least square technique, conditioned to estimated ash category  $c_a$ . The latter is again found by resorting to the forward training model with all potential and limitations discussed for VAC. The choice of the functional relationship may be critical, but, on the other hand, it greatly simplifies the estimation step and makes it computationally very efficient. A power-law regression model can be chosen for ash mass concentration and fall rate for (3) [16], [17]. As listed in Fig. 1, at each time step and for each radar bin, VAE can provide ash mass concentration  $C_a$  ( $\text{g m}^{-3}$ ), ash fall rate  $R_a$  ( $\text{kg m}^{-2} \text{s}^{-1}$ ), mean particle diameter  $D_n$  (mm). If Doppler capability is present and proper algorithms are applied such velocity-azimuth display [42], ash mean velocity  $v_{ma}$  ( $\text{m s}^{-1}$ ) and ash velocity standard deviation  $\sigma_{va}$  ( $\text{m s}^{-1}$ ) in both horizontal and vertical direction can also be estimated. Moreover, some other products can be derived from the overall volume analysis at each time step such as ash plume top height  $H_M$  (m), ash plume volume  $V_a$  ( $\text{m}^3$ ), ash mass loading  $L_a$  ( $\text{kg m}^{-2}$ ), and ash MFR  $F_{Ra}$  ( $\text{kg s}^{-1}$ ). The latter is described in Sect. V.A.

#### B. Volcanic ash detection (VAD) module

Detection of ash clouds is a cumbersome problem, as their signature can be confused, from a microwave radar point of view, with hydrometeor features. In this paragraph a methodology is presented for the real-time automated identification of volcanic solid particle emissions, based on the availability of weather radar data every  $\Delta t$  minutes. The detection (or monitoring) method, here discussed, exploits the analysis of copolar reflectivity measurements associated to geographical digital information. This is justified by the fact that most operational radar systems are single-polarization only so that this choice implies the applicability of our VAD methodology to all weather radars currently used for volcano monitoring. Its generalization to polarimetric radar data is beyond the scopes of this work, but it is of course feasible [17]. The proposed scheme for monitoring and tracking ash plumes is presented in Fig. 2.

As described in section II.A, weather radar data can be integrated with information received from different available sources, such as remote sensors from ground stations, space platform and the Volcanic Aviation Advisory Center (VAAC) bulletin. The efficacy of radar detection and tracking of ash plumes is, of course, conditioned by the optimal choice of radar site, which may limit the volcanic vent microwave visibility.

The VAD algorithm is designed to: i) keep pace with real-time data and to provide a detection result at the end of each radar volume acquisition (as fast as possible in order to follow the eruption dynamics); ii) store previous acquired data (at least 1 hour), to be maintained in a database in order to allow further analyses if needed. Radar algorithms can usually be applied to measurements represented in native spherical coordinates or to data in resampled Cartesian coordinates, which allows a simpler geometrical interpretation. The VAD algorithm, instead of

using the radar 3D volume, is applied to a bidimensional (2D) product, such as the Vertical Maximum Intensity (VMI) which is the maximum value of measured reflectivity along the column at each Cartesian ground pixel  $(x,y)$  or  $(i,j)$  in its discrete form. The advantage of considering VMI is the reduction of the processing complexity, making VAD computationally more efficient. In addition, since VMI privileges the reflectivity peaks that are present in a radar volume, it results more suitable for hazard warning. Obviously, all noise contaminations in radar volumes (e.g., ground clutter, second trip echoes and anomalous propagation effects) must be filtered out in order to efficiently discriminate atmospheric targets. The VAD technique should use the appropriate scan strategy (i.e. the number of elevation-azimuth angles) that is a critical decision during operational use. The choice shall depend on the distance between the volcano and the radar and on the heights of radar beams with respect to the surface.

The VAD algorithm starts splitting the coverage area, where all potentially active volcano vents are located, in three (or more) concentric circular sectors arbitrarily centered on the volcano location. As an example, Fig. 3 shows how the sectors are subdivided for the Mt. Etna (left panel) and the Grímsvötn volcanic target area (right panel). Due to the diverse geographical characteristics and radar installations, the homologous sectors have different sizes in the two analyzed target areas. The basic idea is to mark each concentric circular sector  $s_k$  (e.g.,  $k=1,2,3$ ) with the class labels  $s_k=yes$  (Y) or  $s_k=no$  (N), according to a hybrid fuzzy-logic probabilistic strategy.

The block diagram of VAD algorithm is structured along the following steps:

1. Define concentric circular sectors  $s_k$  of diameters  $d_1 < \dots < d_k < d_{k+1}$  within the radar maximum coverage area and centered on the volcano vent (typically  $k=3$ ).
2. Extract within these sectors  $s_k$  and at each discrete time step  $t_n$  the following features at each pixel  $(i,j)$ : i) reflectivity VMI values  $Z_M(s_k, i, j, t_n)$ ; ii) echo-top height values  $H_M(s_k, i, j, t_n)$  which is the maximum height where  $Z_M(s_k, i, j, t_n) > S_{Zk}$  and where  $S_{Zk}$  is a proper threshold that is empirically derived; iii) the percentage  $N_p(s_k, t_n)$  of  $N_k$  pixels of  $Z_M$  above the threshold signal  $S_{Zk}$  with respect to the total sector pixels  $N_{tot}(s_k)$  so that  $N_p(s_k, t_n) = 100 N_k / N_{tot}(s_k)$  with  $N_k$  larger than a threshold signal  $S_{Zk}$ . This threshold is empirically set and may be site dependent (e.g., see Sect. III and Tab. IV).
3. Convert each feature  $X$  (with  $X=Z_M, H_M$  or  $N_p$ ) into a membership probability using a ramp membership function  $M_X[X; X_{th}, \Delta X]$ . The latter is defined as a function of the threshold parameter  $X_{th}$  and interval parameter  $\Delta X$  so that:

$$\begin{cases} M_X[X; X_{th}, \Delta X] = 0 & \text{if } X < X_{th} \\ M_X[X; X_{th}, \Delta X] = 1 & \text{if } X > X_{th} + \Delta X \\ M_X[X; X_{th}, \Delta X] = \Delta X^{-1}(X - X_{th}) & \text{elsewhere} \end{cases} \quad (4)$$

The values of the thresholds and interval parameters depend on the radar scan strategy, distance volcano-radar and their relative altitude, radar azimuth and range resolution and circular sector topology (e.g., see Sect. III

and Table IV).

4. Define an inference rule function for each sector  $s_k$  as the product of the membership function of each feature  $X$  (*fuzzification stage*):

$$I_k[Z_M, H_M, N_p; s_k] = M_Z[Z_M]M_H[H_M]M_N[N_p] \quad (5)$$

5. Assign a label “Y” (yes) or “N” (no) to each sector  $s_k$  at each time step  $t_n$ , taking the maximum of the inference rule function  $I_k$  and checking if it is greater or lesser than 0.5 (*defuzzification stage*)

$$\text{Max}_{i,j}\{I_k[Z_M, H_M, N_p; s_k]\} = \begin{cases} \geq 0,5 & \rightarrow s_k = Y \\ < 0,5 & \rightarrow s_k = N \end{cases} \quad (6)$$

where the maximum  $\text{Max}_{ij}$  is searched within all pixels  $(i,j)$  of sector  $k$  if the percentage number of pixels is above a given threshold  $S_{Nk}$  that is typically empirically derived.

6. Estimate a probability of ash eruption (PAE) at a given time step  $t_n$  by evaluating different temporal combinations for  $s_k=Y$  or  $N$  at previous time steps  $t_{n-i}$  (with  $i=1 \div N_V$ ) as follows (*ash-eruption conditional probability stage*):

$$PAE(t_n) = p_{ash}(t_n, s_1 | s_2, s_3) p_{avg}(\Delta t_n, s_1 | s_2, s_3) \quad (7a)$$

with

$$\begin{aligned} p_{ash}(t_n, s_1 = Y | s_2, s_3) &> 0 \\ p_{avg}(\Delta t_n, s_1 = Y | s_2, s_3) &= \frac{1}{N_V} \sum_{i=1}^{N_V} p_{ash}(t_{n-i}, s_1 | s_2, s_3) \\ p_{ash}(t_n, s_1 = N | s_2, s_3) &= 0 \end{aligned} \quad (7b)$$

where  $p_{ash}(t_n, s_1=Y | s_2, s_3)$  and  $p_{ash}(t_{n-i}, s_1 | s_2, s_3)$  are the ash conditional probabilities, respectively, at present instant  $t_n$  and at previous acquisition time steps  $t_{n-i}$  for a given class label combination in  $s_1, s_2$  and  $s_3$ , whereas  $N_V$  is the number of volumes considered in previous acquisition time steps within the interval  $\Delta t_n$ . PAE in (7) is the product of two conditional probabilities of ash: the current probability of ash when in the inner sector  $s_1=Y$  and the temporal average of past probabilities in sector  $s_1$ , both conditioned to the outcomes of (5) in outer sectors  $s_2$  and  $s_3$ . Note that the PAE value is computed automatically after every radar volume scan and its value ranges from 0 to 1.

The time span  $\Delta t_n$  of the average probability  $p_{avg}$  is typically set to 1 hour so that  $N_V = \Delta t_n / \Delta t$  with  $\Delta t$  the time step of radar acquisition. Both  $p_{ash}(t_n)$  and  $p_{ash}(t_{n-i})$  are empirically tunable probabilities, depending on the volcanic observation scenario and available information. These conditional probabilities are meant to discriminate ash plumes from meteorological storms exploiting their different temporal evolution. As an example, from the analysis of past case studies of volcanic eruptions in Iceland and Italy, Table I and Table II provide, respectively, the conditional current and previous

probability  $p_{ash}$  in (7), derived from label combinations in sectors 2 and 3 and depending on the label (Y or N) of sector 1. It is worth recalling that, if  $s_1=N$  at current instant  $t_n$ , the PAE value is set to zero automatically. The proposed values in the previous tables basically guarantee that volcanic ash is not detected in cases of persistent and/or widespread radar echoes, likely due to moving stratiform meteorological storms covering the outer sectors in the volcano surrounding. Convective rain clouds, developing close to the volcano vent as in many tropical volcanoes, might be confused with ash plumes. In this respect, radar polarimetry could help in refining the detection procedure. From our experience, for the Icelandic and Italian volcanic eruption cases,  $PAE \geq 0.8$  is associated to the presence of ash plumes, whereas  $PAE \leq 0.6$  are mainly due to meteorological targets. On this basis, as soon as sector 1 is labeled as Y, the PAE value is computed by means of (7).

7. Label the radar echoes around the potential volcanic vent in the inner sector  $s_1$  at instant  $t_n$  by means of  $L_{PAE}(t_n, s_1)$ , defined as (*ash-eruption target labeling stage*):

$$L_{PAE}(t_n, s_1) = \begin{cases} \text{Meteorological} & \text{if } 0 \leq PAE < T_{E1} \\ \text{Uncertain} & \text{if } T_{E1} \leq PAE < T_{E2} \\ \text{Ash} & \text{if } PAE \geq T_{E2} \end{cases} \quad (8)$$

where  $T_{E1}$  and  $T_{E2}$  are proper thresholds, typically set to 0.6 and 0.8 respectively as mentioned before.

8. The spatial identification of radar echoes, affected by ash, can be performed by introducing the Probability of Ash Detection (PAD). The latter is an areal probability of detection applied to all pixels within radar coverage estimated as (*ash-detection conditional probability stage*):

$$PAD(i, j, t_n) = \{w_z M_Z[Z(i, j)] + w_H M_H[H_M(i, j)]\} M_D[d(i, j)] \quad (9)$$

where the new membership function  $M_D$  takes into account the distance between the pixel  $(i,j)$  and the volcano vent. Roughly speaking, (9) reveals the presence of ash in a given pixel if there is a suitable distance from the vent via  $d$ , if those pixels lie in a specified range of altitudes via  $H_M$  and if the maximum reflectivity is sufficiently high via  $Z_M$ . PAD values are in the same range of the PAE; in (9) the weights  $w_z$  and  $w_H$  can be set to 0.5, but they can take into account the instantaneous availability of each source of information and its strength. The PAD formula in (9) may be enriched and improved by exploiting additional radar features, such as spatial texture and gradient of reflectivity, radial velocity as well as some polarimetric features.

9. In similar fashion to (8), we can then define a radar detection label  $L_{PAD}(t_n, i, j)$ , which has generally different thresholds  $T_{E3}$  and  $T_{E4}$ . The  $L_{PAD}$  label is introduced to discriminate among meteorological and ash in each pixel of the radar domain taking into account any uncertain or mixed condition (*ash-detection target labeling stage*):

$$L_{PAD}(t_n, i, j) = \begin{cases} \text{Meteorological} & \text{if } 0 \leq PAD < T_{E3} \\ \text{Uncertain} & \text{if } T_{E3} \leq PAD < T_{E4} \\ \text{Ash} & \text{if } PAD \geq T_{E4} \end{cases} \quad (10)$$

If  $L_{PAE}(t_n, s_1) = \text{Ash}$ , the VAD algorithm switches (automatically or semi-automatically) into a warning mode so that tracking (VAT), classification (VAC) and estimation (VAE) procedures can be activated. These modules are applied to  $(i, j)$  pixels where  $PAD_k(i, j, t_n) \geq T_{E3}$ , in order to keep pixels labeled as ash or as uncertain. The probability PAE in (7), immediately after the ash detection instant  $t_n$ , must be evaluated with **Table III**, instead of **Table I**, in order to verify if the volcanic ash eruption from the vent is a continuing phenomenon.

If  $L_{PAE}(t_n, s_1) = \text{Uncertain}$ , reflectivity echoes can be affected by false alarm or misdetection due to mixed phase (hydrometeor and ash signatures) or under particular atmospheric conditions.

If  $L_{PAE}(t_n, s_1) = \text{Meteorological}$ , VARR-chain successive modules are not activated and the detection cycle is updated to the next time step. Note that, if immediately after  $L_{PAE}(t_n, s_1) = \text{Ash}$ , then  $s_1 = N$  and PAE is set to zero and probably a false alarm may have happened or it may behave intermittently. On the other hand, if the eruption stops after some time, dispersed ash will be detected only into outer sectors but not in the inner sector  $s_1$ . In these cases, VAT, VAC and VAE are applied anyway to  $(i, j)$  pixels where  $PAD(i, j, t_n) \geq T_{E3}$ .

In summary, the probability of the volcanic eruption onset is described in time by the PAE time series evolution. Its behavior is an indicator of **eruption column** ejecting ash in the surrounding of the volcanic vent. On the other hand, the spatial discrimination between ash and meteorological radar echoes is performed by PAD maps. The efficiency of the latter is, of course, essential for any prompt and effective support to decision.

### III. RADAR-BASED DETECTION OF VOLCANIC ERUPTION ONSET

The VAD algorithm has been tested for several volcanic eruptions and requires that a weather radar is available and operating during the eruption, which is not always the case when eruptions occur.

As an example, here we will show the results obtained from the volcanic eruption that occurred on May 2011 at the Grímsvötn volcano, located in the northwest of the Vatnajökull glacier in south-east Iceland (e.g., [27]). It is one of the most active Icelandic volcanoes. An explosive subglacial volcanic eruption started in the Grímsvötn caldera around 19:00 UTC on May 21, 2011. The strength of the eruption decreased rapidly and the plume was below  $\sim 10$  km altitude after 24 h [40]. The eruption was officially declared over on 28 May at 07:00 UTC. More details on the Grímsvötn eruption observations and estimates can be found in [27] and [23] with a comprehensive analysis of the eruptive event from VAC and VAE results using polarimetric radar data at X band.

The X-band dual polarization radar measurements (DPX) used in this study are acquired by the Meteor 50DX system which is a mobile compact weather radar deployed on a transportable trailer. For the volcanic event of May 2011 in Iceland, it has been positioned in the Kirkjubæjarklaustur, southern Iceland, at approximately 75 km from the Grímsvötn volcano [23]. During its operational activities on May 2011, DPX scans were set to 14 elevations angles from  $0.7^\circ$  to  $40^\circ$ . All polarimetric observables have a range, azimuth and time sampling of 0.20 km and  $1^\circ$  and 10 min, respectively and have been properly post-processed to remove ground-clutter and others impairments. A flow diagram of the VARR algorithm chain is shown in **Fig.4**. The data processing steps, applied to this case study and here summarized, are well described in [23].

Three concentric circular sectors, centered at the Grímsvötn eruption vent have been set up having a maximum range of 8, 20 and 60 km respectively (see Fig. 3, right panel). The number of time steps  $N_V$ , to be used in (7), depends on the rate of radar scans; since in this case scans are every 10 minutes, then  $N_V = 6$  within an hour. Results of VAD for this case study are shown in **Fig. 5** and **Fig. 6** on 2 time intervals on the third day, as an example. PAE values have been computed using the processing chain of Sect. II since the beginning of eruption in different weather condition. The label value (Y" or "N") of each sector is also shown for completeness. The maximum values of the detected reflectivity, along the vertical column centered on  $(i, j)$ , are projected on the surface as a Plan Position Indicator (PPI) georeferenced radial map. The label VMI-CZ in these figures stands for vertical maximum intensity corrected reflectivity where the corrections are those usually related to ground-clutter removal and Doppler dealiasing [42].

The ash plume is visible over the Grímsvötn volcano, especially looking at the sequence of Fig. 5 where strong reflectivity values are detected around the vent in clear air conditions. On the contrary, Fig. 6 shows the sequence of PAE values in presence of a small horizontally-extended ash plume coexisting with other meteorological clouds in the outer sectors. The latter may cause false alarms, but the conditional check of all sectors avoids apparent detection errors. The detected volcanic plume is also distinguishable from undesired residual ground clutter returns, the latter being recognizable as it tends to show a VMI stationary field from an image to another.

The temporal sequence of PAE, which might represent an operational warning product of VAD, is shown in **Fig. 7** for whole days of 24 and 25 May. In this figure gray areas indicate the instants where we have found an ash plume by visual inspection of each radar scan. The colored circles in the PAD sequence refer to hit, false and miss plume detection. The hit rate (green circles) is high and this is an encouraging result for further tests. In the case of 2011 Grímsvötn event the observed temporal sequence definitely indicates a distinct ash feature erupted from the volcano vent, which can be effectively detected by means of the PAE product. Missed detection (i.e., observed, but not detected by PAE algorithm) is due to very low reflectivity values around the volcano vent correlated to the small observed plume. False detection could instead occur when rain clouds, developing close to the volcano vent, are

confused with ash plumes.

Some examples of PAD results, computed by (9), are shown in Fig. 8 for some instants selected considering different weather conditions. The results are expressed using the radar detection label  $L_{PAD}$ , in (10), once setting the thresholds  $T_{E3}=0.6$  and  $T_{E4}=0.8$ . As expected, in case of an ash eruption in clear air with strong reflectivity values, as in May 23, 12.21 UTC, the PAD is set to *ash mode*. In the mixed scenario of May 23, 13.30 UTC PAD changes into *uncertain mode*; it is worth noting that the residual ground clutter is classified as a meteorological target, as expected.

#### IV. RADAR AND INFRASOUND DETECTION OF ASH

MW weather radars can scan the whole atmosphere in a 3D fashion in an area of about  $10^5 \text{ km}^2$  [12]. The entire volume is accomplished in about 3 to 5 minutes depending on the number of elevation angles, azimuth angles and range bins, but also on the antenna rotation rate (which is typically of 3 to 6 rounds per minutes). This means a single voxel (volume pixel) of the 3D volume can only be sampled every few minutes. In this respect MW weather radar can benefit from the integration of other volcanic site measurements with a more rapid sampling, but still sensitive to the onset of the ash eruption. This paragraph will explore this synergetic scenario.

The Mt. Etna volcano (Sicily, Italy) has produced more than fifty lava fountains since 2011 from a new crater formed in November 2009 [25], [18]. These events are characterized by the onset of Strombolian activity accompanied by volcanic tremor (resumption phase), an intensification of the explosions with the formation of an eruption column producing ash fallout (paroxysmal phase) and, finally, the decrease of both the explosion intensity and volcanic tremor (final phase) ([20], [25]).

The Mt. Etna eruption of Nov. 23, 2013 was a lava fountain event more intense than usual which began in the afternoon of November 22, intensified after 07:00 UTC of Nov. 23 [26]. The lava fountain formed at 09:30 UTC and lasted up to 10:20 UTC, forming a magma jet up to about 1 km and an eruption plume higher than 9 km that dispersed volcanic ash toward the north-eastern volcano flanks [35]. The eruption ended at about 11:30 UTC.

This Mt. Etna eruption was observed by the same DPX X-band radar system, deployed in Iceland in 2011 (see Set. III). In this case the DPX radar is permanently positioned at the Catania airport (Sicily, Italy) at an altitude of 14 m and approximately 32 km far away from the Mt. Etna crater of interest (see Fig 3a, left panel). The DPX radar system works at 9.4 GHz and is operated to cover an area within a circle of 160 km radius every 10 minutes [23]. Fig. 9 shows temporal samples of VMI imagery showing the onset of the lava fountain at 9:40 UTC, the intensification and the dissipation around 10:40 UTC. Note that the ash plume is not detected by DPX radar after 10:40 UTC since radar is not sensitive to fine ash (with sizes less than about 50-micron diameter) at long range which is indeed dispersed in the north-east direction after the eruption end.

Volcanic activity produces infrasonic waves (i.e. acoustic waves below 20 Hz), which can propagate in the atmosphere

useful for the remote monitoring of volcanic activity [20]. Infrasonic (IS) associated with explosive eruptions is generally produced by the rapid expansion of the gas-particle mixture within the conduit and, in consequence, it is related to the dynamics of the volume outflow and thus to the intensity of the eruption [21], [22]. At Mt. Etna a 4-element IS array (with small aperture of 120-250 m, at an elevation of 2010 m above sea level and at a distance of 5500m from the summit craters) has been operating since 2007 [25]. Each element has a differential pressure transducer with sensitivity of 25 mV/Pa in the frequency band 0.01–50 Hz and a noise level of  $10^{-2}$  Pa. Array analysis is performed by a multichannel semblance grid-searching procedure using a sliding 5-s long window. The expected azimuth resolution is of  $\sim 2^\circ$ , which corresponds to about 190m at a distance of 5.5 km. The IS array mean pressure amplitude  $P_{ISmean}$  of the acoustic signals detected by the array in 5 min long time window is usually computed for data analysis. Details on this installation, operating as part of the permanent monitoring system of Etna volcano, can be found in [25].

Similarly to Fig. 7, Fig. 10 and Fig. 11 show the time series of estimated probability of ash eruption and plume maximum height above the sea level, respectively, derived from the VAD algorithm during the Mt. Etna eruption of Nov. 23, 2013. Instantaneous mean pressure from infrasonic array, sampled every 5 seconds, is also superimposed for the same event. The interesting feature, noted in Fig. 10, is the time shift between the MW radar detection and infrasonic signature. In particular, in this case the time difference between radar-based maximum height  $H_M$  and infrasonic-based  $P_{ISmean}$  peak is about 17 min, the VAE-based maximum plume height above the vent is about 7.9 km, the horizontal distance up to  $H_M$  peak from vent is about 12 km.

This time shift between MW radar and  $P_{ISmean}$  infrasonic is due to the time necessary for the plume to reach its maximum height, and, therefore, is related to the plume rising velocity. Nonetheless, while infrasonic is peaking the increase of pressure at the vent, the radar is detecting the MW maximum values above the vent. Using data shown in Fig. 10 and 11, we can thus estimate the average uprising velocity of the erupted mixture: the vertical component is about 7.7 m/s whereas the horizontal component is about 11.7 m/s. These estimates seem to be consistent with a buoyancy-driven ascent for volcanic plumes such as that on Nov. 23. In summary, this investigation seems to confirm that: i) combination of radar and IS data are ideal ingredients for an automatic ash eruption onset early warning within a supersite integrated system (see Fig. 1); ii) the shift between MW radar and IS array signatures may provide estimate of the mean buoyant plume velocity field.

#### V. MASS FLOW RATE ESTIMATION AT THE VOLCANO VENT

Once the eruption onset is detected by VAD and tracked by VAT, in order to forecast the ash dispersal, it is fundamental to estimate the source mass flow rate at the volcano vent [28]. The plume maximum height, the vertical distribution of erupted mass and the rate of ash injection into the atmosphere, all depend on the MFR, wind entrainment and advection, temperature of the erupted mixture and the atmospheric

stratification [4]. In this respect, both MW radar and infrasound measurements can help and in this section we will compare them with estimates from a parametric analytical model using data of the 2010 of Eyjafjallajökull, eruption [30].

During the eruption in April-May 2010 of Eyjafjallajökull stratovolcano, the ash plume was monitored by a C-band scanning weather radar, managed by IMO (Icelandic Meteorological Office) and located in Keflavik at 155 km from the volcano [14], [15]. The single-polarization Keflavik radar provides the reflectivity factor  $Z_{hhm}$  every 5 minutes. By applying the VAC and VAE of the VARR algorithm (see Fig. 1), we have obtained the ash concentration estimates for each radar bin considered above the volcano vent. The trend of the plume top height shows values between 5 and 6 km above sea level in agreement with other observations [14], [15].

#### A. Radar-based and infrasonic retrieval of source MFR

These VAE-based ash concentration estimates have been used to provide an approximate quantification of source MFR at the vent [31]. The evolution of a turbulent plume formed above the vent during an explosive eruption can be described physically by mass conservation equation within a volume above the vent. By integrating over the columnar volume  $V_c$  within the closed surface  $S_c$  above the vent and using the divergence theorem, we can obtain the radar-based source MFR  $F_{Rrad}$  (kg/s) defined as sum of derivative mass rate  $D_R$  (kg/s) and the mass advection rate  $A_R$  (kg/s) [31]:

$$F_{Rrad}(t) = D_R(t) + A_R(t) \quad (11a)$$

where, if  $\mathbf{r}=[x,y,z]$  is the position vector,  $\mathbf{n}_0$  is the outward normal unit vector and  $\mathbf{v}_a$  is the ash mass velocity field, it holds:

$$\begin{cases} D_R(t) = \iiint_{V_c} \frac{\partial C_a(\mathbf{r},t)}{\partial t} dV \\ A_R(t) = \oint_{S_c} C_a(\mathbf{r},t) [\mathbf{n}_0 \cdot \mathbf{v}_a(\mathbf{r},t)] dS \end{cases} \quad (11b)$$

where  $S_c$  is the surface enclosing the volume  $V_c$  when the mass balance is computed.

By discretizing (11), source MFR can be estimated from weather radar measurements around the volcano vent, imposing the time step  $\Delta t$  equal to the radar scan sampling time (here, 5 minutes) and setting up the horizontal section of the columnar volume  $V_c$  (here, 5x5 pixels with a pixel size of about 1 km per side). The 3D vectorial velocity field  $\mathbf{v}_a(\mathbf{r},t)$  of the divergent advection rate  $A_R$  can be estimated either from radar Doppler moments (if available) or from temporal cross-correlation techniques, such as PCORR (see Sect. II), applied in a 3D fashion. If the advection rate is neglected, then MFR is underestimated as advective outflow tends to remove ash from the column.

MFR can be estimated by means of infrasonic array measurements [19]-[21]. In the far-field conditions (i.e. for acoustic wavelength much larger than source dimension), the linear theory of sound demonstrates that acoustic pressure can be related to the source outflow velocity assuming a monopole, dipole or quadrupole source of sound [34]. Thermal camera imagery suggested that the sound associated with the

Eyjafjallajökull ash plume dynamics is more consistent with the dipole source [19]. Under the assumption that the acoustic velocity of the expanding surface within the conduit is equivalent to the plume exit velocity (as suggested by thermal imagery analysis of Strombolian explosions [43]), for a cylindrical conduit of radius  $R_v$ , the infrasound-based source MFR  $F_{Rifs}$  can be calculated as [19]:

$$F_{Rifs}(t) = 6.768 \cdot \rho_p \cdot R_v^{1.66} \cdot \left( P_{ISmean}(t) \frac{r_s}{\rho_{air}} c \right)^{1/3} \quad (12)$$

where  $R_v$  is the estimated radius of the vent,  $\rho_p$  is the mixture density,  $P_{ISmean}$  is the mean pressure amplitude,  $\rho_{air}$  is the density of the atmosphere,  $c$  the sound speed and  $r_s$  is the distance from the source (see [19] for parameter values). For this case study, the ash plume activity of Eyjafjallajökull in 2010 has been recorded using a 4-element infrasonic array at a distance of 8.3 km from the craters. These sensors were chosen for their wide frequency band, good pressure sensitivity, and low power requirement (about 60 mW). All the array elements were connected to the central station by cables and data were digitized and transmitted via Internet link to the Icelandic Meteorological Office (IMO).

#### B. Analytical and model-based evaluation of source MFR

Another way to estimate MFR from the eruptive plume top height is to resort to simplified parametric empirical formulas (e.g., [4], [6], [36]) and analytical equations (e.g., [28]). In particular,  $H_M$  can be derived from radar scans (even though the finer particles in the upper plume can be missed due to reduced sensitivity) [14], [15], [38]. The source MFR of a volcanic plume is fundamentally related to the plume top height as a result of the dynamics of buoyant plume rise in the atmosphere, but is also affected by atmosphere stratification (buoyancy frequency), cross-wind and humidity [28], [33]. A nonlinear parametric equation to estimate  $F_{Rmod}$  has been derived, to include both local cross-wind and buoyancy frequency conditions at a given instant [28]:

$$F_{Rmod}(t) = a_0 [a_1 H_M^4(t) + a_2 H_M^3(t)] \quad (13)$$

where  $a_0$ ,  $a_1$  and  $a_2$  are coefficients dependent on the gravitational acceleration, air and plume density, air and plume temperature, specific heat capacity of both air and particles, buoyancy frequency, radial entrainment, wind entrainment and wind velocity profile. The application of (13) (from now on defined as D&B analytical model) at given time step  $t$  requires that the atmospheric conditions close to the volcanic vent are known in order to evaluate the plume bending under the wind effects. Under the approximation of horizontal uniformity of free troposphere, these conditions can be derived from the closest radiosounding (RaOb) station. For this case study atmospheric conditions obtained by ECMWF ERA-40 reanalysis at 0.25° resolution interpolated above the Eyjafjallajökull volcano (see Fig. S5 in [28]). The other parameters used in (13) are listed in Table S1 and S2 of [28].

The source MFR, here labelled as  $F_{Rnum}(t)$ , can also be derived from one-dimensional (1D) numerical models, [28]. The latter are based on the theory of turbulent gravitational

convection from a maintained volcanic source taking into account wind and humidity in the atmosphere, based on Morton's theory [37]. Results from 1D numerical models can be obtained by Monte Carlo simulations run over a large parameter space of **source conditions** (temperature, exit velocity, exsolved gas mass fraction, vent radius, vent height), atmospheric conditions (temperature, wind, and humidity profiles), and radial and wind entrainment coefficients [28]. From this ensemble of 1D Monte Carlo simulation a minimum and maximum value of  $F_{Rnum}(t)$  can be derived at each time step. For these simulations we used the same parameters and atmospheric conditions as in (13), but also take into account the humidity atmosphere (see Fig. S5 in [28]). The source conditions used can be found in Table S2 in [28].

### C. Intercomparison results

The temporal trend of the VARR-based MFR  $F_{Rrad}(t)$ , for the period of May 5-10, 2010, is shown in **Fig. 12** by comparing  $F_{Rrad}(t)$  obtained with and without the **advection term in (11a)** at 10-minute sampling as well as every half hour, 1 hour and 3 hours. The MFR variability, as detected and estimated by the weather radar, shows a pulsed behavior of the MFR at shorter time scales [31]-[32]. Note that the oscillations of VARR-based MFR estimates may be affected by the time sampling of the radar and the volume scan time interval, which is accomplished in a few minutes, whereas the ash plume parameters can vary on the order of a few seconds.

Neglecting the advection term in (10) may lead to a MFR underestimation on average less than an order of magnitude or, in terms of percentage fractional difference, larger than 100% (see middle panel of Fig. 12). This VARR-derived MFR variability is about two order of magnitudes at 10-minute sampling and about an order of magnitude after 1-hour averaging with a mean value around  $5 \cdot 10^5$  kg/s within the observed period. The radar-based capability to catch the MFR intermittent behavior is, to a certain extent, expected as it closely correlates with the pulsating explosive activity through the estimate of the ash mass change and advection [32]. It is worth noting that MFR estimates from field data during the period between 4 and 8 May have provided average values between  $0.6$  and  $2.5 \cdot 10^5$  kg/s [28], [30], not too far from VARR-based MFR variability around its mean value (see Fig. 12). VARR-based MFR values are also higher than those estimated by near-field video analyses between  $2.2$  and  $3.5 \cdot 10^4$  kg/s [36], but closer to those derives from other plume height models between  $26.2$  and  $43.6 \cdot 10^4$  kg/s [36], [33].

**Fig. 13** shows MFR temporal trends in terms of the minimum and maximum values of  $F_{Rnum}(t)$ , derived from the Monte Carlo 1D numerical model using radiosonde available every hour, compared to the minimum and maximum values of  $F_{Rrad}(t)$ , derived from VARR-based algorithm taking every 10 minutes within a running window of 60 minutes. The average value of 1D-model MFR is about  $10^5$  kg/s within the observed period, whereas minimum values are cut at  $10^2$  kg/s, lower values indicating that there were significant humidity effects. This only affects the minimum MFR estimate. The peak-to-peak variability of VARR-derived estimates of MFR is typically between  $10^4$  and  $10^6$  kg/s with episodes down to  $10^3$  kg/s between around May 9. Radar-based MFR tends to be larger than that exhibited by the 1D numerical model, except in a few

cases where the 1D model shows much lower minimum values. These low values can be, for the most part, attributed to the strong humidity effects in the period after May 8, 2010. Due to the change in heat capacity and latent heat release associated with condensation, even plumes with very low mass flow rates can obtain the observed heights [28]. Additionally, there is a larger variability of the plume tops in this period, whose minimum values tend to be much lower than those before May 8.

Fig. 13 also shows the intercomparison among the 1-hour sampled temporal trends of  $F_{Rrad}(t)$ ,  $F_{Rmod}(t)$  and  $F_{Rifs}(t)$ , that is, respectively, MFR estimates obtained from the VARR radar algorithm (expressed as a 1-hour average together with its standard deviation), from the D&B analytical model, (i.e. using (13) applied to the minimum and maximum radar-retrieved plume height every hour; see [28] for details), from the 1D numerical model and from infrasonic array data. Both MFR estimates VARR radar and infrasound estimates of averaged MFR are in quite good agreement being the infrasound estimate within the standard deviation of radar-based MFR around  $10^6$  kg/s. The D&B analytical model tends to provide a lower MFR especially after May 8, 2010. This behavior is strictly linked to the radar estimate of the plume top height  $H_M$  in (13), which tends to be lower in the observation period [29], [14], [15]. Indeed, radar estimates of  $H_M$  may be an underestimation of the true plume top height due to the reduced sensitivity to particles size finer than 50 microns and to the possible occlusions of observation sectors due to ground clutter.

It is also worth noting that, even at the same time sampling of 1 hour, VARR-based estimates of source MFR exhibit a higher intermittency with respect to 1D-model and infrasound estimates with a MFR variability larger than one order of magnitude (this variability is increased up to 2 order of magnitudes at 10-minute sampling in Fig. 12). This feature, which should be confirmed by future investigations, might be related to the fact that the VARR-derived MFR is strictly linked to the mass change rate and its advection, whereas 1D-model estimates depend on the plume top height (which may respond in a slower source flux changes) and infrasound estimates are indirectly correlated to the source MFR through the measured acoustic wave pressure. Furthermore, the uncertainty in the observed parameters of these methods is amplified by the uncertainty of the model parameters used in (12), (13), and the 1D model. In the case of the 1D plume model and the analytical expression (13), for example, the results can be very sensitive to the choice of entrainment coefficients [44].

## VI. CONCLUSION

A hybrid algorithm, named VAD that exploits weather radar data, has been presented to detect the onset of the explosive volcanic eruption and estimate the mass flow rate at the volcano vent. The VAD approach, part of the VARR methodology, can provide the probability of ash detection (PAD) within the radar coverage area and the probability of ash eruption (PAE) at the fissure. Estimates of PAE have been provided for two eruption case studies, in Iceland on 2011 and in Italy in 2013. The quantitative analysis show very encouraging results in terms of detection and labeling which can be useful for any support decision system dealing with volcanic eruption hazard. The

PAE index can be usefully exploited as a diagnostic tool for an early warning integrated platform, which can be of interest for civil prevention and protection. Assuming to pursue a self-consistent radar approach, a way to improve PAE is to also exploit in case of uncertain labeling: i) spatial texture of ash field radar observables versus rain field around the volcano vent; ii) temporal evolution of the radar observables around the volcano vent; iii) Doppler spectrum (mean and spectral width) variability in time and space around the volcano vent; iv) vertical section (RHI) of measured reflectivity along the radar-vent cross section; v) detection of a strong reflectivity gradient (both in space and time) due to ash cloud; vi) use of some polarimetric observables, such as  $Z_{dr}$ , since for tumbling ash particles  $Z_{dr} \approx 0$  for any concentration and diameter, whereas for strong reflectivity ash may have  $K_{dp}$  values near or less than zero as opposed to rainfall. Correlation coefficient should have low values above and around volcano vent in case of eruption being a great mixture of non-spherical particles.

This work has also explored, using the Italian case study in 2013, the synergy between microwave weather radars and infrasonic array observations. The latter have been already used for detecting Etna lava fountains with a high degree of confidence thus demonstrating to be an essential tool for volcanic eruption early warning. Before designing an integrated tool, the interpretation of the respective signatures needs to be investigated and this has been the goal of the presented analysis. Results indicate that the response of the weather radar and infrasonic array to the eruption onset of the plume is correlated and characterized by a time lapse due to the plume rise. The different time sampling of the 2 measurements, typically 10 and 1 minute for radar and infrasound respectively, should be taken into consideration when trying to derive eruption dynamical parameters. If confirmed by further case analyses, the synergy of weather radar and infrasonic array can be framed within the VAD hybrid algorithm by introducing a proper conditional probability of PAE driven by infrasonic array data. This may help VAD to remove ambiguous mixed-phase conditions where the ash plume is coexisting with the meteorological clouds.

Finally, VARR-based retrievals of the source MFR at the vent have been analyzed for a further event in Iceland in 2010 by comparing with estimates of a 1D numerical model, an analytical formula and infrasonic array data. The estimate of source MFR is considered a fundamental step to characterize the volcanic source, but very difficult to measure accurately. Thus, this work for the first time has proposed the intercomparison between 2 experimental techniques, based on weather radar and infrasonic array data, supported by the analyses of 2 modeling approaches. The results show a substantial agreement about the average estimate of MFR from both instruments with the VARR-based showing a larger variability probably due to the source pulse intermittency. The 1D-model variability is within the peak-to-peak estimate of VARR, whereas the wind-driven analytical model can underestimate MFR due to the limits in the estimation of top plume height by radar. Five minutes time resolution appears to be a good compromise to estimate 1-h average mass flow rate and its standard deviation and to allow a complete volume radar

scan.

Further work is required to assess the usefulness of VAD on a statistical basis using a significant number of case studies as well as to couple it with collocated infrasonic array pressure measurements. Unfortunately, only few volcanic sites are nowadays equipped with both instruments and the historical dataset is very limited so far. The probability of ash eruption value and relative spatial identification by means of synergetic PAE and PAD values can be displayed continuously on a devoted web site. Positions of potentially active volcanoes should be displayed as an overlay on monitoring screens. Seismic data can complement the VARR scheme as a priori data in the VAD radar detection module. We expect them to be less correlated to the eruption onset, but they can corroborate and increase the VAD probability of detection. L-Band Doppler radar monitoring with a fixed beam aiming near the source can be easily ingested in the detection procedure (an example can be the Voldorad L-band system near the Etna volcano). Other data, coming from ground-based and space-based remote sensors, can be also combined within VARR in order to provide a comprehensive quantitative overview of the evolving eruption scenario and its source parameters, useful for supporting the decisions of the interested Volcanic Ash Advisory Center.

#### ACKNOWLEDGMENT

We are very grateful to B. Pálmason, H. Pétursson and S. Karlsdóttir (IMO, Iceland) for providing X and C-band Iceland radar data and G. Vulpiani and P. Pagliara (DPC, Italy) for providing X-band Italian radar data. The application of VARR chain algorithms, developed in C language and Matlab® environment, can be discussed with the authors upon request.

#### REFERENCES

- [1]. Miller, T.P., Casadevall, T.J., Volcanic ash hazards to aviation. In: Sigurdsson, H., Houghton, B.F., McNutt, S.R., Rymer, H., Stix, J. (Eds.), *Encyclopedia of Volcanoes*. Academic Press, San Diego, pp. 915–930, 2000.
- [2]. O'Regan, M., On the edge of chaos: European aviation and disrupted mobilities. *Mobilities* 6 (1), 21–30, 2011.
- [3]. Prata, A.J. and Tupper, A., Aviation hazards from volcanoes: the state of the science. *Nat. Hazards*, 2009. <http://dx.doi.org/10.1007/s11069-009-9415-y>.
- [4]. Sparks, R. S. J., Bursik, M. I., Carey, S. N., Gilbert, J. S., Glaze, L., Sigurdsson, H., and Woods, A.W., *Volcanic plumes*. New York, Wiley, 1997.
- [5]. Stohl, A., Prata, A. J., Eckhardt, S., Clarisse, L., Durant, A., Henne, S., Kristiansen, N. I., Minikin, A., Schumann, U., Seibert, P., Stebel, K., Thomas, H. E., Thorsteinsson, T., Tørseth, K., and Weinzierl, B., "Determination of time- and height-resolved volcanic ash emissions and their use for quantitative ash dispersion modeling: the 2010 Eyjafjallajökull eruption", *Atmos. Chem. Phys.*, vol. 11, pp. 4333–4351, doi:10.5194/acp-11-4333-2011, 2011.
- [6]. Mastin, L.G., Guffanti, M., Servranckx, R., Webley, P., Barsotti, S., Dean, K., Durant, A., Ewert, J.W., Neri, A., Rose, W.I., Schneider, D., Siebert, L., Stunder, B., Swanson, G., Tupper, A., Volentik, A., Waythomas, C.F., "A multidisciplinary effort to assign realistic source parameters to models of volcanic ash-cloud transport and dispersion during eruptions". *J Volcanol. Geoth. Res.* vol. 186, pp. 10-21, 2009.
- [7]. Rose, W.I., G. J. S. Bluth, and G. G. J. Ernst, "Integrating retrievals of volcanic cloud characteristics from satellite remote sensors: A summary", *Philos. Trans. Roy. Soc. London*, A358, 1538–1606, 2000.

- [8]. Prata, A. J. and Grant, I. F.: Retrieval of microphysical and morphological properties of volcanic ash plumes from satellite data: Application to Mt. Ruapehu, New Zealand, *Q. J. Roy. Meteorol. Soc.*, 127, 2153–2179, 2001.
- [9]. Pavolonis, M. J., Wayne, F. F., Heidinger, A. K., and Gallina, G. M.: A daytime complement to the reverse absorption technique for improved automated detection of volcanic ash, *J. Atmos. Ocea. Technol.*, 23, 1422–1444, 2006.
- [10]. Harris, D. M. and W. I. Rose, “Estimating particle sizes, concentrations, and total mass of ash in volcanic clouds using weather radar”. *J. Geophys. Res.*, vol. 88, C15, pp. 10969–10983, 1983.
- [11]. Lacasse, C., S. Karlsdóttir, G. Larsen, H. Soosalu, W. I. Rose, and G. G. J. Ernst, “Weather radar observations of the Hekla 2000 eruption cloud”, *Iceland. Bull. Volcanol.*, vol. 66, 5, pp. 457–473, 2004.
- [12]. Marzano F.S., E. Picciotti, G. Vulpiani and M. Montopoli, "Inside Volcanic clouds: Remote Sensing of Ash Plumes Using Microwave Weather Radars", *Bulletin Am. Met. Soc. (BAMS)*, pp. 1567-1586, DOI: 10.1175/BAMS-D-11-00160.1, October 2013
- [13]. Marzano, F.S., S. Barbieri, E. Picciotti and S. Karlsdóttir, Monitoring sub-glacial volcanic eruption using C-band radar imagery. *IEEE Trans. Geosci. Rem. Sensing*, 48, 1, 403-414, 2010.
- [14]. Marzano, F. S., M. Lamantea, M. Montopoli, S. Di Fabio and E. Picciotti, The Eyjafjallajökull explosive volcanic eruption from a microwave weather radar perspective, *Atmos. Chem. Phys.*, 11, 9503-9518, 2011.
- [15]. Arason, P., Petersen G. N. and Björnsson H., Observations of the altitude of the volcanic plume during the eruption of Eyjafjallajökull, April-May 2010, *Earth Syst. Sci Data* 3, 9-17, 2011.
- [16]. Marzano, F. S., S. Barbieri, G. Vulpiani and W. I. Rose, “Volcanic ash cloud retrieval by ground-based microwave weather radar”. *IEEE Trans. Geosci. Rem. Sens.*, vol. 44, pp. 3235-3246, 2006.
- [17]. Marzano F.S., E. Picciotti, G. Vulpiani and M. Montopoli, “Synthetic Signatures of Volcanic Ash Cloud Particles from X-band Dual-Polarization Radar”, *IEEE Trans. Geosci. Rem. Sens.*, vol. 50, pp. 193-211, 2012.
- [18]. Scollo, S., Prestifilippo, M., Spata, G., Agostino, M.D, Coltelli, M., Monitoring and forecasting Etna volcanic plumes, *Nat. Hazards Earth Syst. Sci.* 9, 1573–1585, 2009.
- [19]. Ripepe, M., Bonadonna C., Folch A., Delle Donne D., Lacanna G. and Voight B., Ash-plume dynamics and eruption source parameters by infrasound and thermal imagery: the 2010 Eyjafjallajökull eruption, *Earth and Planetary Science Letters* 366, 112-121, 2013. <http://dx.doi.org/10.1016/j.epsl.2013.02.005>.
- [20]. Jeffrey, B., Jonson, Aster R. C. and Kyle P.R., Volcanic eruptions observed with infrasound, *Geophysical Research Letters*, Vol.31, L14604, doi: 10.1029/2004GL020020, 2004.
- [21]. Caplan-Auerbach, J., Bellesiles A. and Fernandes J. K., Estimates of eruption velocity and plume height from infrasonic recordings of the 2006 eruption of Augustine Volcano Alaska, *Journal of Volcanology and Geothermal Research*, 2009. doi: 10.1016/j.jvolgeores.2009.10.002.
- [22]. Ripepe, M., De Angelis S., Lacanna G. and Voight B., Observation of infrasonic and gravity waves at Soufrière Hills Volcano, Monserrat, *Geophysical Research Letters*, Vol. 37, L00E14, doi: 10.1029/2010GL042557, 2010.
- [23]. Montopoli M., G. Vulpiani, D. Cimini, E. Picciotti, and F.S. Marzano, “Interpretation of observed microwave signatures from ground dual polarization radar and space multi frequency radiometer for the 2011 Grímsvötn volcanic eruption”, *Atmos. Meas. Tech.*, ISSN: 1867-1381, vol. 7, pp. 7, 537–552, 2014.
- [24]. Marzano F.S., M. Lamantea, M. Montopoli, B. Oddsson and M.T. Gudmundsson, “Validating sub-glacial volcanic eruption using ground-based C-band radar imagery”, *IEEE Trans. Geosci. Rem. Sens.*, ISSN: 0196-2892, vol. 50, pp. 1266-1282, 2012.
- [25]. Olivieri G., M. Ripepe, and E. Marchetti, “Infrasound reveals transition to oscillatory discharge regime during lava fountaining: Implication for early warning”, *Geophysical Research Letters*, VOL. 40, 1–6, doi:10.1002/grl.50592, 2013.
- [26]. Corradini S., M. Montopoli, L. Guerrieri, M. Ricci, S. Scollo, L. Merucci, F.S. Marzano, S. Pugnaghi, M. Prestifilippo, L. Ventress, R.G. Grainger, E. Carboni, G. Vulpiani, M. Coltelli, “A multi-sensor approach for the volcanic ash cloud retrievals and eruption characterization”, *Rem. Sensing*, under review, 2015.
- [27]. Marzano, F.S., M. Lamantea, M. Montopoli, M. Herzog, H. Graf, and D. Cimini, “Microwave remote sensing of the 2011 Plinian eruption of the Grímsvötn Icelandic volcano”, *Remote Sens. Environ.*, vol. 129, pp. 168–184, 2013.
- [28]. Degruyter, W. and Bonadonna C., Improving on mass flow rate estimates of volcanic eruptions, *Geophysical Res. Lett.*, Vol.39, L16308, doi: 10.1029/2012GL052566, 2012.
- [29]. Björnsson, H., Magnússon S, Arason P, Petersen G.N., 2013 Velocities in the plume of the 2010 Eyjafjallajökull eruption. *J Geophys Res Atmos* 118:1–14. doi:10.1002/jgrd.50876.
- [30]. Bonadonna, C., Genco R., Gouhier M., Pistolesi M., Cioni R., Alfano F., Hoskuldsson A. and Ripepe M., Tephra sedimentation during the 2010 Eyjafjallajökull eruption (Iceland) from deposit, radar, and satellite observations, *J. Geophys. Res.*, VOL. 116, B12202, doi: 10.1029/2011JB008462, 2011.
- [31]. L. Mereu , Marzano, F.S. ; Montopoli, M. ; Bonadonna, C., “Retrieval of Tephra Size Spectra and Mass Flow Rate From C-Band Radar During the 2010 Eyjafjallajökull Eruption, Iceland”, *IEEE Trans. Geosci. Rem. Sens.*, pp. 5644-5660, 2015.
- [32]. Kaminski, E., Tait S., Ferrucci F., Martet M., Hirn B. and Husson P., Estimation of ash injection in the atmosphere by basaltic volcanic plumes: the case of the Eyjafjallajökull 2010 eruption, *Journal Of Geophysical Research*, Vol. 116, B00C02, doi: 10.1029/2011JB008297, 2011.
- [33]. Woodhouse, M.J., A.J. Hogg, J.C. Phillips and R.S.J. Sparks, “Interaction between volcanic plumes and wind during the 2010 Eyjafjallajökull eruption, Iceland”, *J. Geophys. Res. Solid Earth*, 118, 92–109, doi:10.1029/2012JB009592, 2013.
- [34]. Lighthill, M.J., *Waves in Fluids*. Cambridge University Press, New York, pp.504, 1978.
- [35]. Andronico D., S. Scollo, A. Cristaldi , “Unexpected hazards from tephra fallouts at Mt Etna: The 23 November 2013 lava fountain”, *Journal of Volcanology and Geothermal Research*, vol. 304, pp. 118-125, 2015.
- [36]. Dürig T., M.T. Gudmundsson, S. Karmann, B. Zimanowski, P. Dellino, M. Rietze and R. Büttner, “Mass eruption rates in pulsating eruptions estimated from video analysis of the gas thrust-buoyancy transition—a case study of the 2010 eruption of Eyjafjallajökull, Iceland”, *Earth, Planets and Space*, vol. 67:180, DOI 10.1186/s40623-015-0351-7, 2015.
- [37]. Morton, B. R., G. T. Taylor, and J. S. Turner, “Turbulent gravitational convection from maintained and instantaneous sources”, *Proc. R. Soc. London, Ser. A*, vol. 234, pp. 1–23, 1956.
- [38]. Oddsson B., Gudmundsson, M. T., Larsen, G., and Karlsdóttir, S., “Monitoring of the plume from the basaltic phreatomagmatic 2004 Grímsvötn eruption—application of weather radar and comparison with plume models”, *Bulletin of Volcanology*, v. 74, no. 6, p. 1395-1407, doi:10.1007/s00445-012-0598-9, 2012.
- [39]. Van Eaton, A.R., Mastin, L. G., Herzog, M., Schwaiger, H. F., Schneider, D. J., Wallace, K. L., and Clarke, A. B., “Hail formation triggers rapid ash aggregation in volcanic plumes”, *Nature Communications*, v. 6, p. 7860, doi:10.1038/ncomms8860, 2015.
- [40]. Petersen, G.N., Björnsson, H., Arason, P., and von Löwis, S., “Two weather radar time series of the altitude of the volcanic plume during the May 2011 eruption of Grímsvötn, Iceland”, *Earth System Science Data*, v. 4, no. 1, p. 121-127, doi:10.5194/essd-4-121-2012, 2012.
- [41]. Montopoli, M., F.S. Marzano, E. Picciotti, and G. Vulpiani, “Spatially-adaptive Advection Radar Technique for Precipitation Mosaic Nowcasting”, *IEEE J. Selected Topics in Appl. Rem. Sens.*, ISSN: 1939-1404, vol. 3, pp. 874-884, 2012.
- [42]. Sauvageot, H., *Radar Meteorology*. Norwood, MA: Artech House, 1992.
- [43]. DelleDonne, D., and Ripepe, M., High-frame rate thermal imagery of Strombolian explosion: implication of infrasonic source dynamics. *J. Geophys. Res.*, 117, B09206, <http://dx.doi.org/10.1029/2011JB008987>, 2012.
- [44]. Bonadonna, C., M. Pistolesi, R. Cioni, W. Degruyter, M. Elissondo, and V. Baumann, “Dynamics of wind-affected volcanic plumes: The example of the 2011 Cordón Caulle eruption, Chile”, *J. Geophys. Res. Solid Earth*, 120, doi:10.1002/2014JB011478, 2015.

**Frank S. Marzano** (S’89–M’99–SM’03–F’15) received the Laurea degree (*cum laude*) in Electrical Engineering (1988) and the Ph.D. degree (1993) in Applied Electromagnetics both from the University of Rome “La Sapienza”, Italy. In 1992 he was a visiting scientist at Florida State University, Tallahassee, FL. During 1993 he collaborated with the Institute of Atmospheric Physics, National Council of Research (CNR), Rome, Italy. From 1994 till 1996, he was with the Italian Space Agency, Rome, Italy, as a post-doctorate researcher. After being a lecturer at the University of Perugia, Italy, in 1997 he joined the Department of Electrical Engineering, University of L’Aquila, Italy teaching

courses on electromagnetic fields as Assistant Professor. In 1999 he was at Naval Research Laboratory, Monterey, CA, as a visiting scientist. In 2002 he got the qualification to Associate Professorship and has co-founded Center of Excellence on Remote Sensing and Hydro-Meteorological Modeling (CETEMPS), L'Aquila. In 2005 he finally joined the Dept. of Information engineering, Electronics and Telecommunications, Sapienza Univ. of Rome, Italy where he presently teaches courses on antennas, propagation and remote sensing. Since 2007 he is vice-director of CETEMPS of the University of L'Aquila, Italy where he became Director in 2013. His current research concerns passive and active remote sensing of the atmosphere from ground-based, airborne, and space-borne platforms and electromagnetic propagation studies. Dr. Marzano has published more than 110 papers on refereed International Journals, more than 30 contributions to international Book chapters and more than 230 extended abstract on international and national congress proceedings. He was the Editor of 2 books. Since January 2004 he has been acting as an *Associated Editor* of IEEE Geoscience Remote Sensing Letters. In 2005 and 2007 he has been Guest Co-Editor of the MicroRad04 and MicroRad06 Special Issues for IEEE-GRSL. Since January 2011 he is Associate Editor of the journal EGU Atmospheric Measurements Techniques. He is a Fellow of the UK Royal Meteorological Society and member of the MWI-ICI Science Advisory Group of EuMetSat and PMM Science Team of NASA.

**Errico Picciotti** received the Laurea degree (*cum laude*) in electrical engineering from the University of Ancona, Ancona, Italy, in 1993. In 1997, he was with the Science and Technology Park of Abruzzo, L'Aquila, Italy, as a Radar Meteorologist. In 2002, he was a Researcher with the CETEMPS, University of L'Aquila, L'Aquila, Italy, where he worked on radar systems and polarimetry. Since 2007, he has been with HIMET, L'Aquila, where he is the Manager of the Radar Meteorology Division. His main research interests are devoted to radar meteorology and volcanic plume retrieval algorithms.

**Saverio Di Fabio** received the Laurea degree (*cum laude*) in electrical engineering from the University of L'Aquila, Italy. In 1998 he joined the Science and Technology Park of Abruzzo, L'Aquila, Italy, as a Microwave Engineer. From 2009 till 2012 he has been with HIMET, L'Aquila as a Radar engineer. Since 2012 he is a Senior scientist with CETEMPS, University of L'Aquila, L'Aquila, Italy, where he has been working on radar systems and polarimetric data processing.

**Mario Montopoli** received the Laurea degree in Electronic Engineering in 2004 from the University of L'Aquila, Italy. In 2005 he joined the Center of Excellence CETEMPS as a research scientist on ground-based radar meteorology and microwave remote sensing. In 2006 he was a research assistant at the Dept. of Electrical Engineering and Information of the University of L'Aquila, Italy. In 2005 he started a Ph.D. program on radar meteorology within a joint program between the University of Basilicata and Sapienza University of Rome, obtaining the degree in 2008. Since October 2011 till 2013 he is with the Dept. of Geography of the University of Cambridge (UK) under the Marie Curie FP7 European program. He is currently with the Dept. of Information Engineering of Sapienza University of Rome and EuMetSat Visiting Scientist at H-SAF facility.

**Luigi Mereu** received the B.Sc. in telecommunication engineering and the M.Sc. degree in telecommunication engineering from Sapienza University of Rome, Italy, in 2007 and 2012, respectively. In 2012 he joined the Department of Information Engineering at Sapienza University of Rome, Italy and the Centre of Excellence CETEMPS in L'Aquila to cooperate on radar remote sensing of volcanic ash clouds within the ICT Ph.D. program. He is involved within the FUTUREVOLC European project started in 2012. He received the IEEE GRS South Italy award for the Best Master Thesis in remote sensing in 2012.

**Wim Degruyter** is currently a Senior scientist at the Institute of Geochemistry and Petrology, Department of Earth Sciences, Zurich, CH. He received the Master of Engineering Science from University of Ghent in 2006 and the PhD in Earth Science in 2010 at the University of Geneva, Switzerland. He has been Post-doctoral researcher at the University of California, Berkeley, USA and Post-doctoral researcher between 2010-2012 at the Georgia Institute of Technology, USA till 2015. His main research interests are devoted to the development of 1-D models to simulate bubble growth, magma chamber dynamics, magma ascent dynamics, and volcanic plume behavior.

**Costanza Bonadonna** is an associate professor at the Department of Earth Sciences of the University of Geneva and Head of the CERG-C Program for

the Assessment and Management of Geological and Climate related risk. She received her B.S. degree in Geology from the University of Pisa, Italy, and Ph.D. degree from the University of Bristol, U.K. She was then awarded the position of SOEST Young Investigator at the University of Hawaii for two years and was later appointed the position of Assistant Professor at the University of South Florida. Costanza Bonadonna was a recipient of the President's Award of the Geological Society of London (2001), the IAVCEI Outstanding Recent Graduate (George Walker Award) (2004), the Outstanding Woman in Science Award of the Geological Society of America (2004), and the USF Outstanding Faculty Research Achievement Award (2005). She has devoted most of her research to modeling sedimentation from volcanic plumes, exploring new methodologies for the characterization of tephra-fall deposits, and developing probabilistic analyses for the assessment of tephra-fall hazards. She is now also involved in several multidisciplinary projects for the quantification of risk.

**Maurizio Ripepe** is currently with the Department of Earth Science, University of Florence, Florence (Italy) teaching Earth Physics and Volcanic Hazard. He has been lecturer in Geophysics and Seisology at the University of Camerino and Siena (1993-2005), external Professor at the Open University, Milton Keans (UK, 2001-2004), visiting Fellow at the University of Southern California (USA, 1986-1989) and visiting Professor at the University of Hokkaido, Sapporo (Japan, 2000), Ecole Normal Supérieure de Physique, Lyon (France, 2002), University of Tohoku, Sendai (Japan, 2007) and Earthquake Research Institute, Tokyo (Japan, 2009). He is also affiliated researcher at the Earthquake Research Institute (ERI) di Tokyo (Japan, 2011). His main research interests are within geophysics and volcanology with a focus on volcanic plumes, volcanic hazard, infrasound techniques and field campaign activities.

## LIST OF TABLES

**Table I.** Conditional probability  $p_{ash}$  for sector 2 and 3 once sector 1 is marked as Y ( $s_1=Y$ ) at present instant  $t_n$  or at previous instants  $t_{n-i}$ . Note that, if  $s_1=N$  at current instant  $t_n$ , PAE value is set to zero automatically. The rationale behind is that volcanic ash is not detected in cases of persistent and/or widespread radar echoes due to meteorological clouds.

Label combination if $s_1=Y$	Sector 3 labeled as $s_3=Y$	Sector 3 labeled as $s_3=N$
Sector 2 labeled as $s_2=Y$	$p_{ash}(t_n, s_1=Y   s_2=Y, s_3=Y) = 0.00$	$p_{ash}(t_n, s_1=Y   s_2=Y, s_3=N) = 0.50$
Sector 2 labeled as $s_2=N$	$p_{ash}(t_n, s_1=Y   s_2=N, s_3=Y) = 0.70$	$p_{ash}(t_n, s_1=Y   s_2=N, s_3=N) = 1.00$

**Table II.** Conditional probability  $p_{ash}$  for sector 2 and 3 once sector 1 is marked as N ( $s_1=N$ ) at previous instants  $t_{n-i}$

Label combination if $s_1=N$	Sector 3 labeled as $s_3=Y$	Sector 3 labeled as $s_3=N$
Sector 2 labeled as $s_2=Y$	$p_{ash}(t_{n-i}, s_1=N   s_2=Y, s_3=Y) = 0.00$	$p_{ash}(t_{n-i}, s_1=N   s_2=Y, s_3=N) = 0.75$
Sector 2 labeled as $s_2=N$	$p_{ash}(t_{n-i}, s_1=N   s_2=N, s_3=Y) = 0.65$	$p_{ash}(t_{n-i}, s_1=N   s_2=N, s_3=N) = 1.00$

**Table III.** Conditional probability  $p_{ash}$  for sector 2 and 3 if sector 1 is marked  $s_1=Y$  at current and previous instants  $t_{n-i}$  and if  $PAE \geq 0.80$  (ash echo).

Label combination if $s_1=YES$ and $PAE(t_{n-1})$ seems to confirm an eruption	Sector 3 labeled as $s_3=Y$	Sector 3 labeled as $s_3=N$
Sector 2 labeled as $s_2=Y$	$p_{ash}(t_n, s_1=Y   s_2=Y, s_3=Y) = 0.4$	$p_{ash}(t_n, s_1=Y   s_2=Y, s_3=N) = 0.9$
Sector 2 labeled as $s_2=N$	$p_{ash}(t_n, s_1=Y   s_2=N, s_3=Y) = 0.75$	$p_{ash}(t_n, s_1=Y   s_2=N, s_3=N) = 1$

**Tab. IV.** Parameters of the VAD membership functions  $M_X$ , as described in (4), in the three sectors for the 2011 Grímsvötn case study.

Symbol	Parameter	Units	Value in sector $s_1$ ( $k=1$ )	Value in sector $s_2$ ( $k=2$ )	Value in sector $s_3$ ( $k=3$ )
$Z_{Mth}$	VMI reflectivity	dBZ	20	20	15
$\Delta Z_M$	VMI reflectivity interval	dBZ	10	10	10
$H_{Mth}$	Max altitude	km	0.8	1.4	1.4
$\Delta H_M$	Max altitude interval	km	1	0.6	0.6
$N_{pth}$	Percentage pixel number threshold	(a) %	0	0	0
$\Delta N_p$	Percentage pixel number interval	(b) %	100	40	10
$S_{zk}$	VMI reflectivity threshold	dBZ	20	15	10
$S_{Nk}$	Pixel number threshold	Adim.	3	8	100
$N_{tot}(s_k)$	Total pixel number	Adim.	5021	26392	216384

LIST OF FIGURES

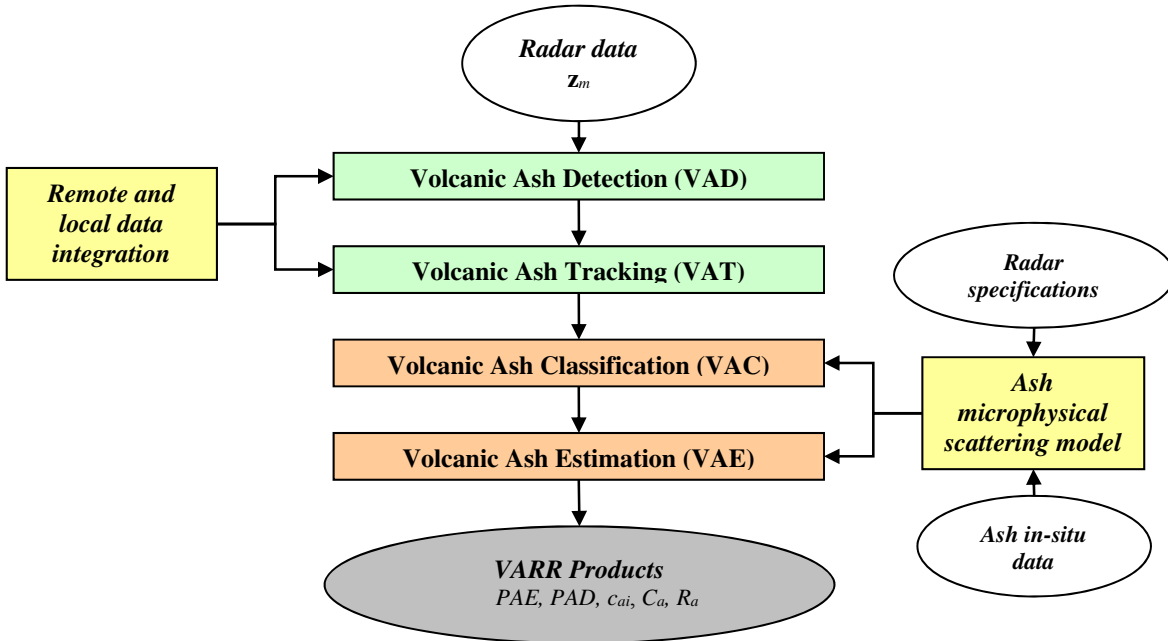


**Fig. 1** At each time step and for each radar bin VARR can provide probability of ash eruption PAE [%] and detection PAD [%], ash classification  $c_{ai}$  (i.e., mean particle diameter  $D_n$  (mm)), ash mass concentration  $C_a$  ( $\text{g m}^{-3}$ ) and ash fall rate  $R_a$  ( $\text{kg m}^{-2} \text{s}^{-1}$ ). If Doppler capability are present, ash mean velocity  $v_{ma}$  ( $\text{m s}^{-1}$ ) and ash velocity standard deviation  $\sigma_{va}$  ( $\text{m s}^{-1}$ ) can be also estimated. Moreover, some other useful products could be derived such as ash plume top height  $H_M$  (m), ash erupted volume  $V_a$  ( $\text{m}^3$ ), ash mass loading  $L_a$  ( $\text{kg m}^{-2}$ ), and ash mass flow rate  $F_{Ra}$  ( $\text{kg s}^{-1}$ ).

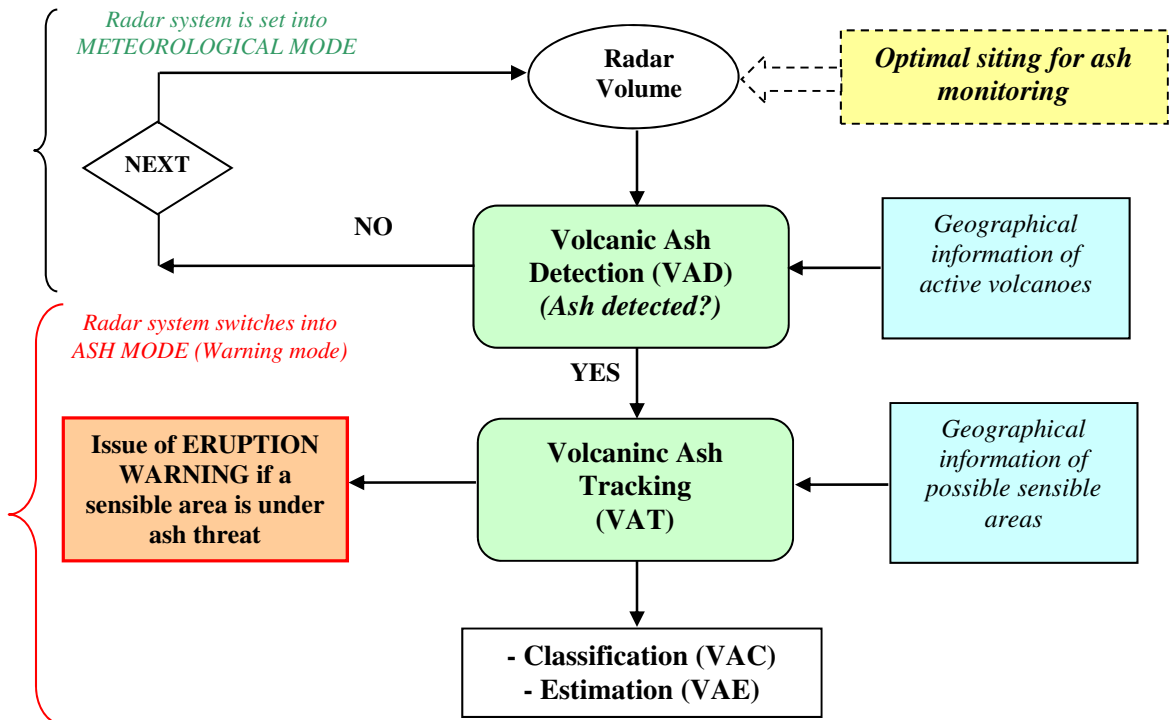


**Fig. 2** Schematic block diagram for ash detection (VAD) coupled with tracking (VAT), classification (VAC) and estimation (VAE) modules. Radar 3D volumes are available typically every 5, 10 or 15 minutes, depending on the range-elevation-azimuth scanning schedule and system specifications.

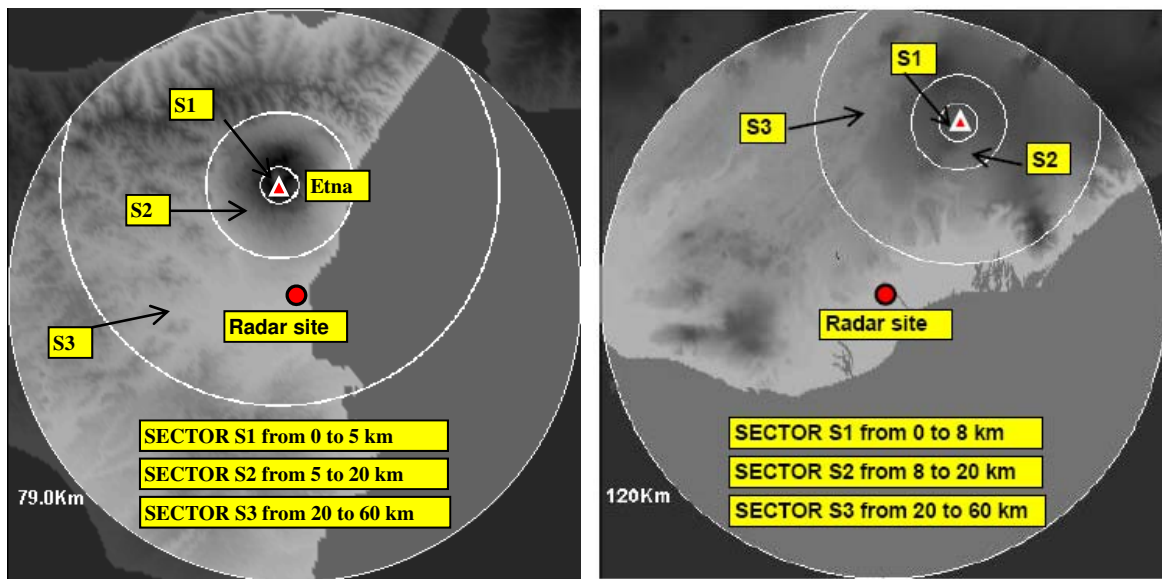


**Fig. 3** The three sectors in which the Mt. Etna volcanic area (left panel) and Grímsvötn volcanic area (right panel) are subdivided. Circular sectors  $s_1$ ,  $s_2$  and  $s_3$  have different radii in the two areas due to different setups and, within each of them, radar observables are processed by the VAD algorithm.

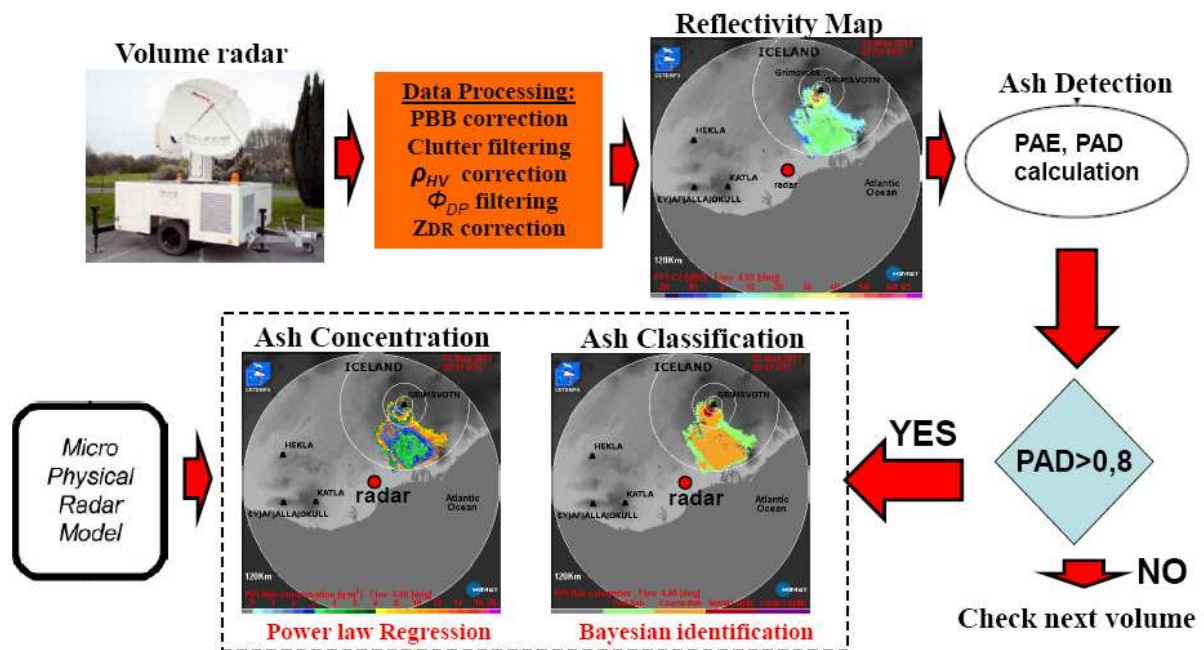


**Fig. 4** VARR data processing flow diagram as applied to the 2011 Grímsvötn eruption case study (see text for details). Acronyms and symbols: PAE (Probability of ash eruption), PAD (Probability of ash detection), PBB (partial beam blocking).  $Z_{hh}$  is the measured copolar reflectivity factor,  $Z_{dr}$  the differential reflectivity,  $\Phi_{dp}$  the phase shift,  $\rho_{hv}$  is copolar correlation (modulus).

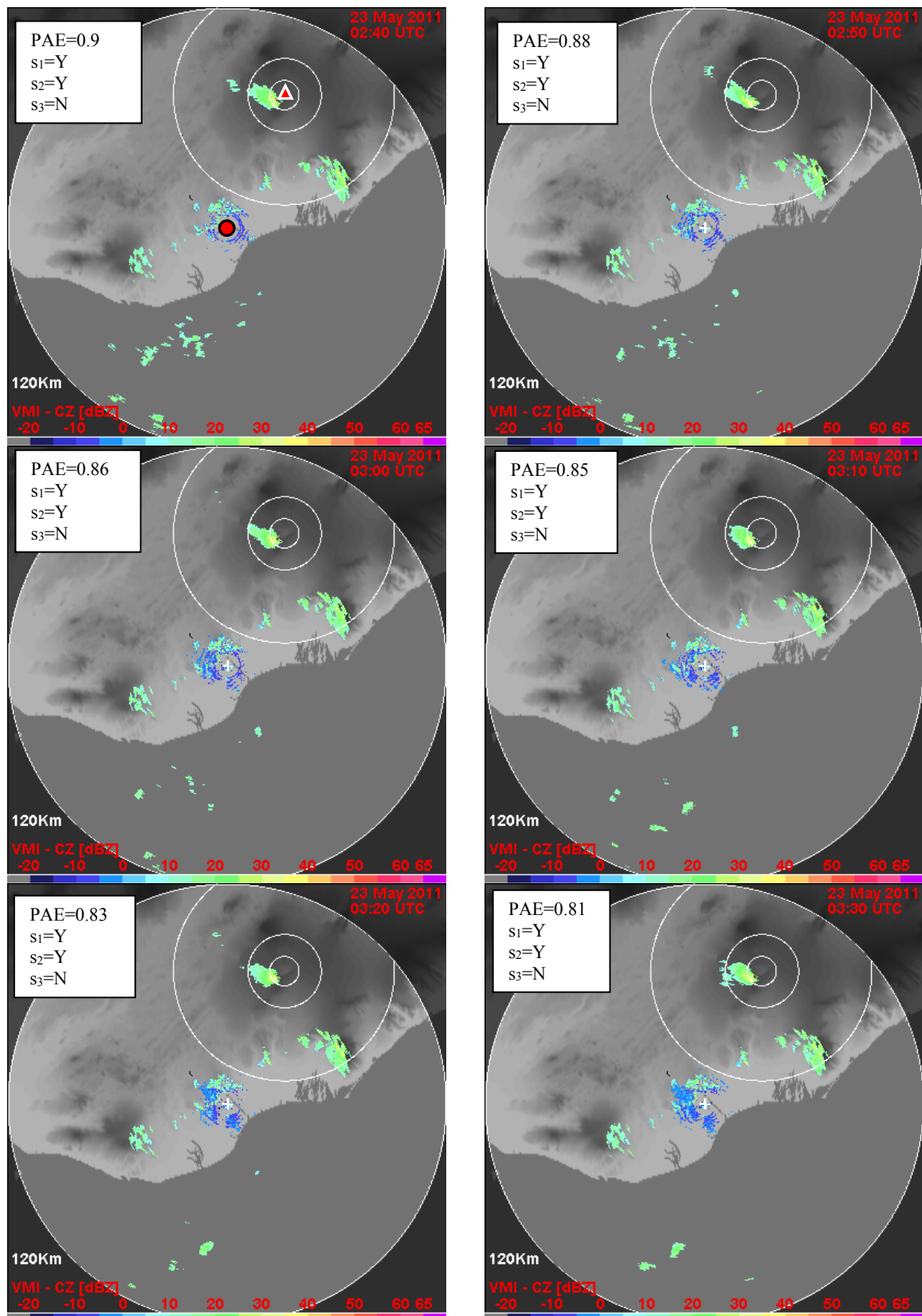


**Fig. 5** Vertical Maximum Intensity (VMI) of corrected reflectivity (CZ), taken by Meteor 50DX on May 23 from 02:40 till 03:30 UTC during the 2011 Grímsvötn eruption. The radar and the volcano vent positions are indicated only in the first panel, with the red circle and red triangle symbols, respectively. PAE and sector label values for each sector are also shown. Signals outside  $s_1$ ,  $s_2$  and  $s_3$  domains are mainly due to clutter.

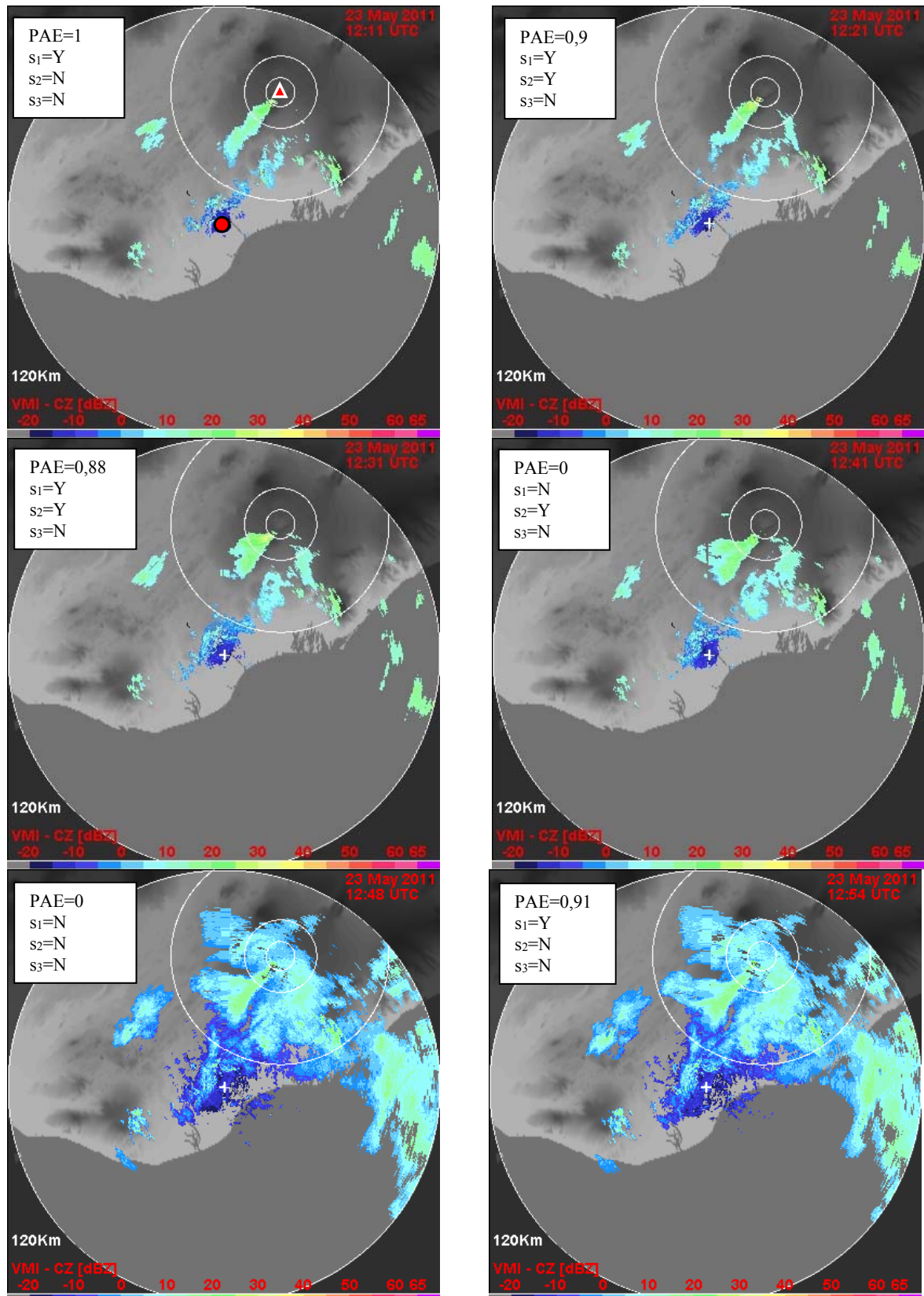


**Fig. 6** Corrected VMI reflectivity images taken by Meteor 50DX on May 23 from 12:11 till 12:54 UTC during the 2011 Grímsvötn eruption. The radar and the volcano vent positions are indicated only in the first panel, with the red circle and red triangle symbols, respectively. PAE and sector=label values for each sector are also shown.

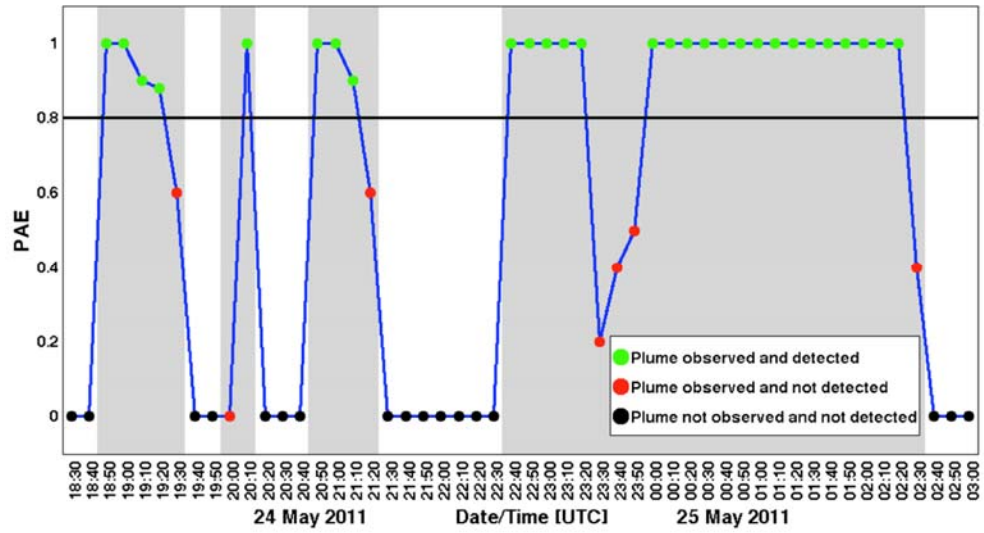


**Fig. 7** Temporal sequence (sampled every 10 minutes) of PAE, extracted by VAD from X-band radar images on May 24-25, 2011 during the Grímsvötn eruption. Grey areas mark instants where a posteriori visual inspection confirmed the presence of the plume at the Grímsvötn volcano.

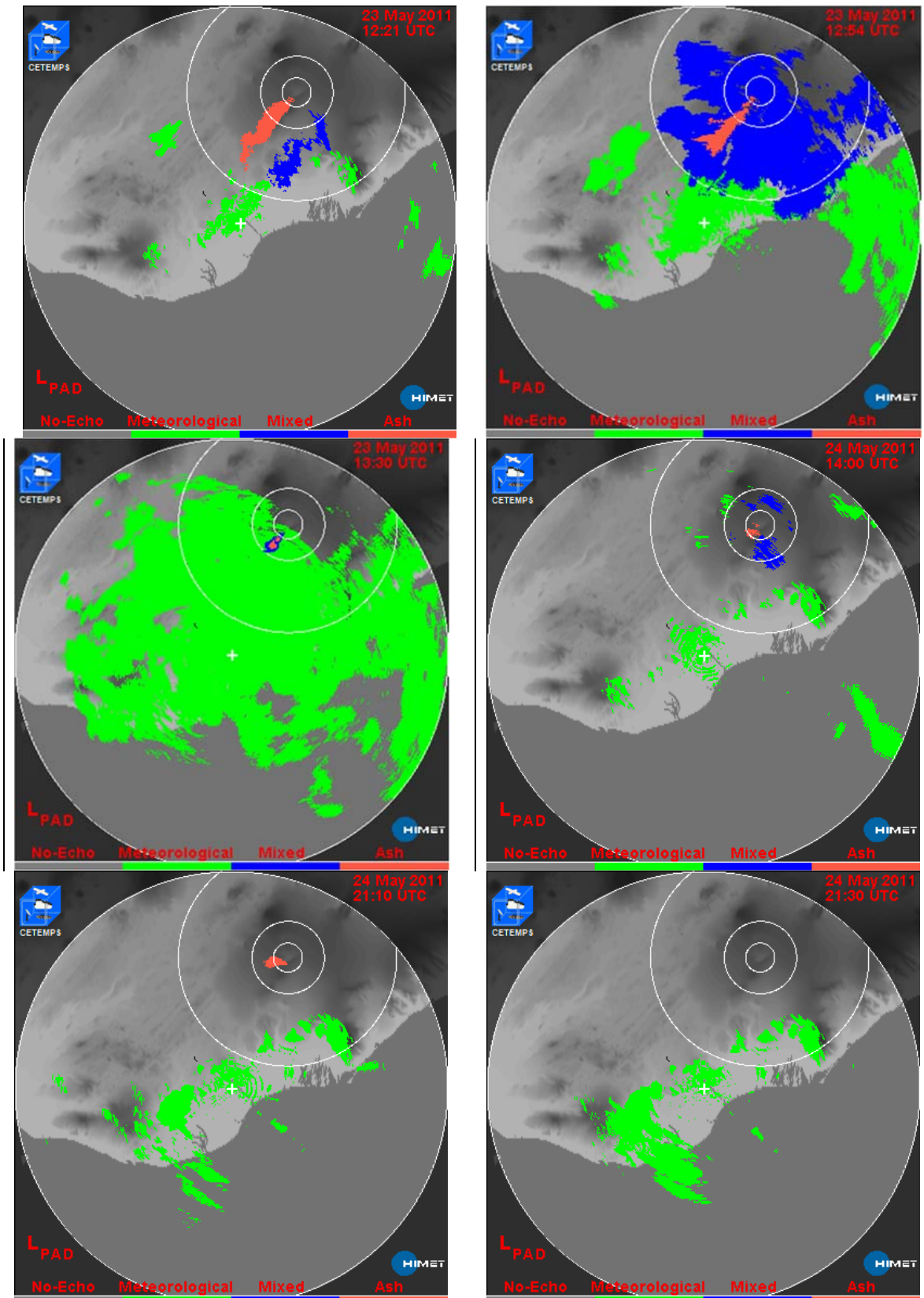


**Fig. 8** Example of VAD results using the probability-of-ash-detection label  $L_{PAD}$  for some eruption instants, selected considering different weather condition during the 2011 Grímsvötn eruption.

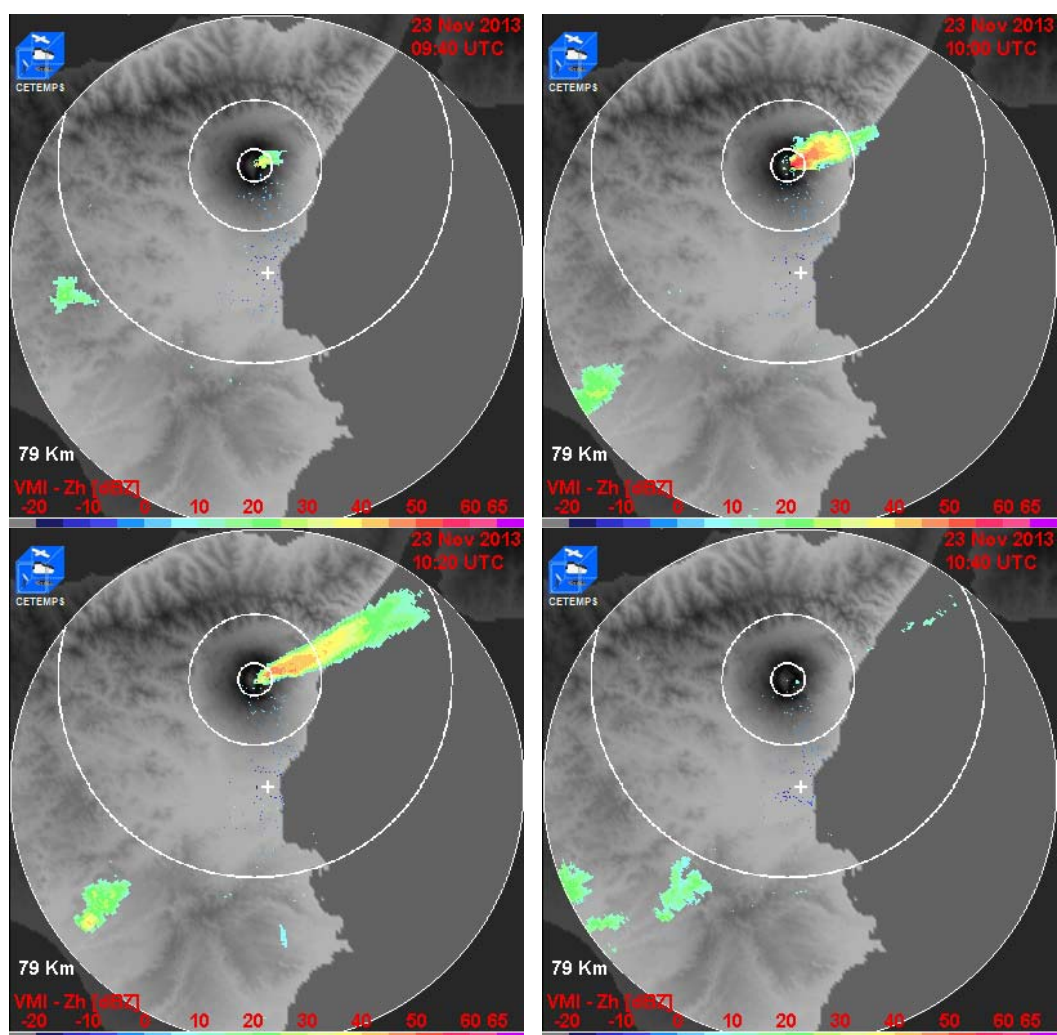


**Fig. 9** VMI images, as derived from X-band DPX radar system located at the Catania airport, during the Mt. Etna eruption on Nov. 23, 2013. Only time steps at 9:40, 10:00, 10:20 and 10:40 UTC are shown for brevity.

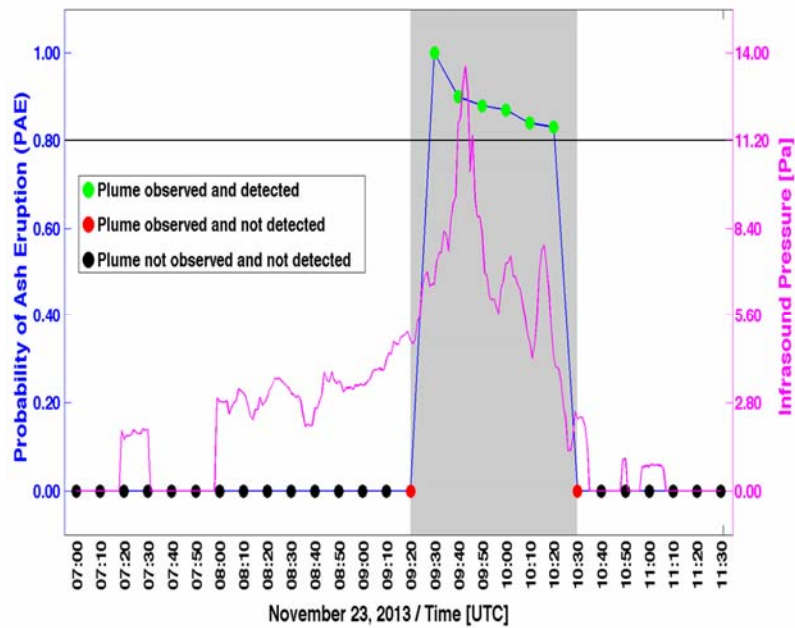


**Fig. 10** Temporal sequence (blue curve) of estimated probability-of-ash-eruption (PAE), sampled every 10 minutes as extracted by VAD from X-band radar data, on Nov. 23, 2013 during the Mt. Etna eruption. Grey areas mark instants where PAE was labelled “Ash” and visual inspections confirmed the presence of an ash plume. Instantaneous mean pressure from IS array (pink curve), sampled every 5 s and temporally averaged with 5-minute window, is also shown.

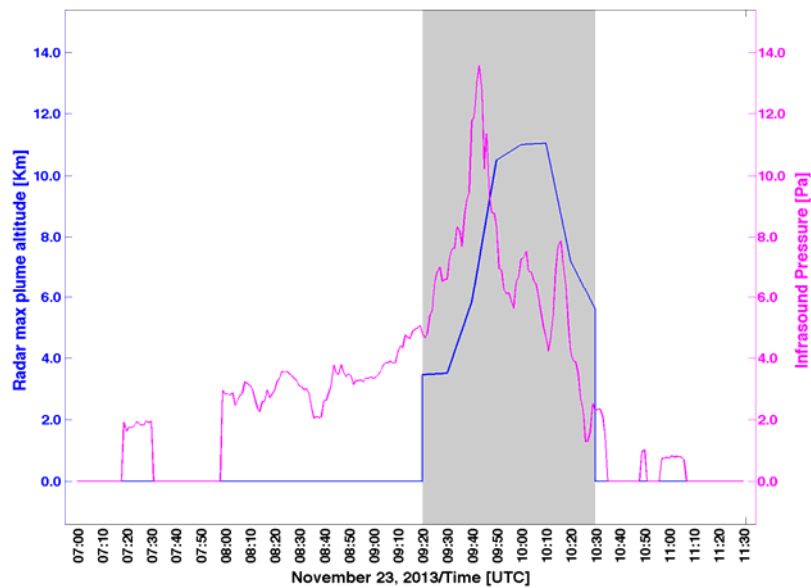


**Fig. 11.** Same as in Fig. 10, but for the plume maximum height above-the-sea-level derived from VARR.

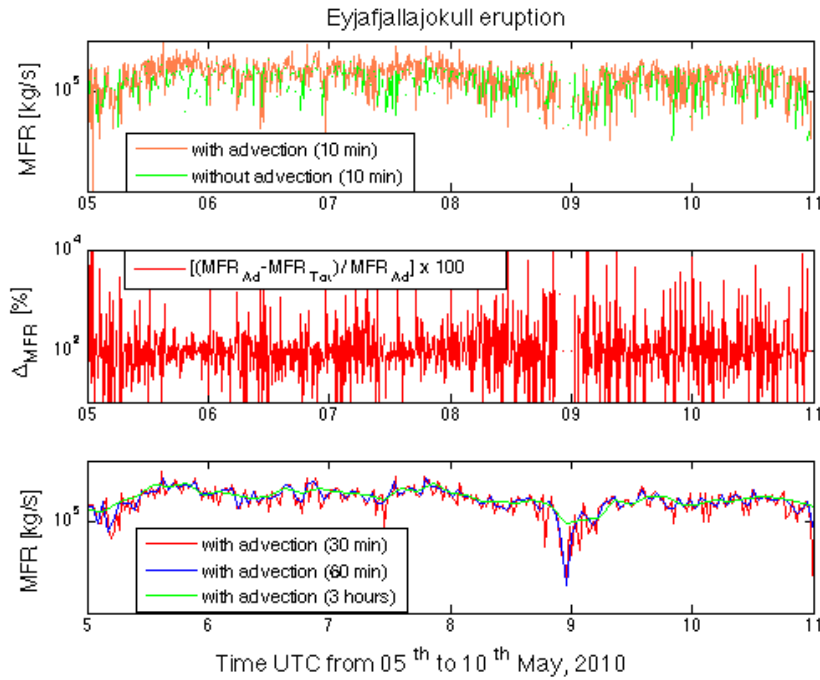


**Fig. 12.** (Top panel) Temporal trend of radar-derived MFR, estimated considering in (11) the  $A_R$  advection term (orange line) and without advection term (green line), within the eruption period of 5-10 May 2010 (Mid panel) Percentage fractional difference between radar-derived MFR with advection and MFR without advection term, normalized to MFR with advection (Bottom panel) Averaged VARR-derived MFR, obtained considering the advection term, with a running time window of 30, 60 and 180 minutes (red, blue and green line respectively).

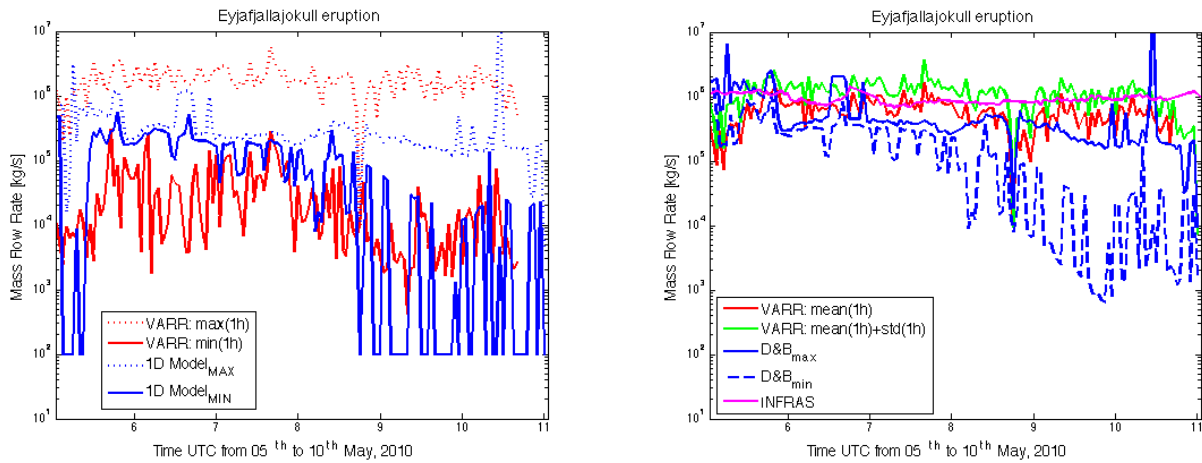


**Fig. 13.** (Left panel) As in Fig. 12, but showing the 1D numerical model MFR minimum and maximum values (derived from Monte Carlo simulations using available radiosonde data) compared with VARR-based MFR minimum and maximum values, obtained from VARR radar algorithm within a running window of 1 hour. (Right panel) Intercomparison among the 1-hour sampled temporal trends of MFR obtained from i) VARR radar algorithm using an average of 60 minutes (red line) with its standard deviation (green line), ii) the D&B analytical model, applied to the minimum and maximum radar-retrieved plume height within 1 hour (blue line), iii) infrasound (INFRAS) array data (pink line). See text for details.